

**Poynting Flux Dominated Jets in Decreasing Density Atmospheres.  
I. The Non-relativistic Current-driven Kink Instability  
and the Formation of “Wiggled” Structures**

Masanori Nakamura<sup>1</sup> and David L. Meier

*Jet Propulsion Laboratory  
California Institute of Technology  
Pasadena, CA 91109*

Masanori.Nakamura@jpl.nasa.gov

**ABSTRACT**

Non-relativistic three-dimensional magnetohydrodynamical (MHD) simulations of Poynting flux dominated (PFD) jets are presented. Our study focuses on the propagation of strongly magnetized hypersonic, but sub-Alfvénic ( $C_s^2 \ll V_{\text{jet}}^2 < V_A^2$ ) flow and on the subsequent development of a current-driven (CD) kink instability. This instability may be responsible for the “wiggled” structures seen in sub-parsec scale (VLBI) jets. In the present paper, we investigate the nonlinear behavior of PFD jets in a variety of external ambient magnetized gas distributions, including those with density, pressure, and temperature gradients. Our numerical results show that the jets can develop CD distortions in the trans-Alfvénic flow case, even when the flow itself is still strongly magnetically dominated. An internal non-axisymmetric body mode grows on time scales of order of the Alfvén crossing time and distorts the structure and magnetic configuration of the jet. The kink ( $m = 1$ ) mode of the CD instability, driven by the radial component of the Lorentz force, grows faster than other higher order modes ( $m > 1$ ). In the jet frame the mode grows locally and expands radially at each axial position where the jet is unstable: the instability, therefore, does not propagate as a wave along the jet length. CD instabilities have a number of features that make them an attractive explanation for the helical jet structure observed in AGN and pulsars: 1) because the magnetic field remains strong, CD instabilities do not develop into full MHD turbulence; 2) the helical structures saturate and advect with the

---

<sup>1</sup>NRC Research Fellow

bulk flow; 3) they distort the body of the jet, not merely its interface with the ambient medium; 4) local plasma flow, then, follows a helical path along the kinked magnetic field backbone. A naturally-occurring, external helically magnetized wind, which is (quasi-) axially current-free, surrounds the well-collimated current-carrying jet and reduces velocity shear between the jet and external medium. This stabilizes the growth of MHD Kelvin-Helmholtz surface modes in the inner jet flow.

*Subject headings:* Instabilities—galaxies: active—galaxies: jets— methods: numerical—magnetohydrodynamics (MHD)

## 1. INTRODUCTION

Magnetohydrodynamic (MHD) acceleration mechanisms often are invoked as a model for the launching and initial acceleration and collimation of winds and jet outflows from Young Stellar Objects (YSOs), X-ray binaries (XRBs), Active Galactic Nuclei (AGNs), Microquasars, and Quasars (QSOs) (see, *e.g.*, Meier, Koide, & Uchida 2001, and references therein). There has been a growing recognition in recent years, however, that the influence of strong magnetic fields within the jet may extend well beyond the central engine into the region where the jet freely propagates, influenced only by internal and ambient hydro- and magnetohydrodynamic forces. This is particularly evident in observations of jets in AGNs, QSOs, winds from pulsars, and  $\gamma$ -ray burst sources (GRBs) (*e.g.*, Perley, Bridle, & Willis 1984; Conway & Murphy 1993; Hester et al. 2002; Coburn & Boggs 2003).

Strongly magnetized jets, particularly those with a strong toroidal field encircling the collimated flow, are often referred to as “current-carrying” or “Poynting flux dominated” (PFD) jets. A large current flowing parallel to the jet flow is responsible for generating a strong, tightly-wound helical magnetic field. Continued rotation of the entire magnetized plasma about the jet axis also plays an important role in jet dynamics. Rotation of the helical field drives a “barber pole”-like, torsional Alfvén wave (TAW) forward in the direction of the jet flow, carrying electromagnetic energy and further accelerating the plasma. In a PFD jet, the Poynting flux energy carried by this TAW can greatly exceed the kinetic energy flux in the hydrodynamic (HD) part of the flow.

It is well-known that a cylindrical plasma column with a helical magnetic configuration is subject to MHD instabilities. These are usually divided into pressure-driven (PD), Kelvin-Helmholtz (KH), and current-driven (CD) instabilities (see *e.g.*, Kadomtsev 1966; Bateman 1980; Freidberg 1982, for details). PD instabilities are related to the interplay between gas pressure and curvature of magnetic field lines (Kersalé, Longaretti, & Pelletier 2000; Longaretti 2003), and have not been considered to be very important for a supersonic jet. KH instabilities occur because of the pres-

ence of velocity gradients in the flow (see *e.g.*, Landau & Lifshitz 1959; Chandrasekhar 1961, for details). They may play an important role at the shearing boundary between the flowing jet and external medium, particularly in kinetic flux dominated (KFD) jets where the hydrodynamical forces dominate over magnetic. PFD jets, on the other hand, should be especially susceptible to CD instabilities because of the presence of the strong axial electric current. The investigation into the destructive influence of CD instabilities on jet flow, therefore, recently has become an important avenue of research in the study of astrophysical jets.

The purpose of the present paper is an in-depth, 3-D MHD, non-relativistic numerical investigation of the nonlinear development of CD instabilities in PFD jets — particularly the CD kink ( $m = 1$ ) mode. Our jets are endowed with most of the properties now thought to characterize those in AGN, QSOs, pulsars, and GRBs: strongly magnetized, hyper-sonic (but sub-Alfvénic;  $C_s^2 \ll V_j^2 < V_A^2$ ) flow, driven by a Poynting flux dominated, torsional Alfvén wave that carries most of the energy. In a previous paper (Nakamura, Uchida, & Hirose 2001), the basic behavior of TAWs and PFD jets was studied under simplified atmospheric conditions. We now assume more realistic atmospheric situations, including density, pressure, magnetic field, and temperature gradients in the ambient medium. While these jets are strictly “*propagating*” (we do not consider the central engine itself), it is important to realize that the inclusion of toroidal magnetic fields and rotation can create a local acceleration and collimation process within the jet that can increase the speed of the jet downstream up to and beyond the Alfvén speed. *Unlike previous studies of propagating jets, therefore, the downstream properties of the jet will be determined not only by the flux of kinetic energy injected at the jet throat (i.e., the initial jet speed and Mach number), but also by the amount of Poynting flux injected in the TAW itself.*

In section 2, we give a review of observational and theoretical work on the subject, relating previous results to the current work. Section 3 outlines our basic numerical methods and model. Section 4 gives a comprehensive report and discussion on our results. Our conclusions are summarized in section 5.

## 2. MAGNETOHYDRODYNAMIC vs. HYDRODYNAMIC JETS

### 2.1. Observational Evidence for Strongly Magnetized Jets

There are several observational results which indicate the presence of strong magnetic fields in astrophysical jets. The first class of observations concerns the structure of the magnetic field. In the case of AGN jets, this is determined from radio polarization of the synchrotron emission, especially the Rotation Measure (RM) and the projected magnetic field vectors (*e.g.*, Perley, Bridle, & Willis 1984; Owen, Hardee, & Cornwell 1989; Perlman et al. 1999; Feretti et al. 1999; Eilek

& Owen 2002; Krause & Löhr 2004). Asada et al. (2002) showed that the RM distribution for the quasar 3C 273 jet on parsec scales has a systematic gradient across the jet, and the projected magnetic field vector is systematically tilted from the direction of the central axis of jet. They conclude that the sign reversal of the RM across jet indicates the presence of a toroidal (azimuthal) component of the field inside jet. In the case of  $\gamma$ -ray burst (GRB) jets, Coburn & Boggs (2003) observed linear polarization in the prompt  $\gamma$ -ray emission from GRB021206 and found a value of  $80 \pm 20\%$ . This is the theoretical maximum possible polarization for a magnetized plasma, indicating that the field is so strong that the entire  $\gamma$ -ray-emitting region is organized around the field structure. The flow clearly is magnetically dominated, and the authors further suggest that the GRB explosion itself is powered by magnetic fields.

A second class of observations concerns the morphological structure of the jets themselves. High resolution VLBI observations show that many AGN and quasar jets display wiggles or kinks on sub-parsec to parsec scales (*e.g.*, Krichbaum et al. 1990, 1992; Hummel et al. 1992; Conway & Murphy 1993; Roos, Kaastra, & Hummel 1993; Jones et al. 1996; Krichbaum et al. 1998; Mantovani et al. 1999; Murphy et al. 1999; Hutchison, Cawthorne, & Gabusda 2001; Lobanov & Zensus 2001; Stirling et al. 2003). Such a helical distortion might be caused either by MHD instabilities, or by precession of the jet ejection axis due to the existence of a binary Black Hole (BBH) (Begelman, Blandford, & Rees 1980), or by an encounter with another galactic core. On the other hand, the precession and galaxy interaction models tend to operate on rather long ( $10^8$  yr) time scales, while the kinks appear to occur on significantly shorter ( $\ll 10^7$  yr) time scales (*e.g.*, Potash & Wardle 1980). Based on both theoretical considerations and observational results, therefore, MHD instabilities appear to be the most plausible model for the observed wiggled or kinked structures.

The third indicator of possible dynamical importance of magnetic fields is the presence of thermal overpressures in jets. There are several such cases in which the jet thermal pressure significantly exceeds the surrounding X-ray gas pressure (see *e.g.*, Potash & Wardle 1980; Owen, Hardee, & Cornwell 1989; Birkinshaw & Worrall 1993). The required self-confinement of this pressure is easily understood in terms of the magnetically-dominated jet model. The toroidal field component  $B_\phi$  provides collimation of the MHD jet and confinement of high pressure gas via the “hoop-stress” ( $-B_\phi^2/4\pi r$ ), which is a part of the magnetic tension force  $[(\mathbf{B} \cdot \nabla)\mathbf{B}]$ .

## 2.2. Basic Structure of a Current-carrying Jet

The global picture of a current-carrying jet with a closed current system linking magnetosphere and hot spots, was introduced by Benford (1978) and applied to AGN double radio sources. A closed current system includes a pair of current circuits, each containing both a forward elec-

tric current path (the jet flow itself, with its toroidal magnetic field, toward the lobe), and a return electric current path (along some path back to the AGN core). The stability of current-carrying jets for two types of return current distributions have been discussed: (1) the returning currents are assumed to flow within the jet itself (the jets are thermally confined by external medium) (Chiuderi, Pietrini, & Torricelli-Ciamponi 1989), and, (2) the returning currents are assumed to flow around the jet, such as in a magnetized cocoon (Benford 1978).

### 2.3. Stability of HD Jets

Most of the early work on jet stability concentrated on the purely hydrodynamical (HD) KH stability for simple configurations such as “top-hat” velocity profiles (Gill 1965; Hardee 1979, 1983; Payne & Cohn 1985; Hardee & Norman 1988; Zhao et al. 1992a; Hardee & Stone 1997) and other flows (see *e.g.*, Birkinshaw 1991; Ferrari 1998, and references therein). Two types of KH waves are considered disruptive in jets: the fundamental surface wave and the reflected body wave (Bodo & Ferrari 1982; Zhao et al. 1992a). Surface mode waves are excited in the presence of non-zero velocity gradients and/or discontinuities at the boundaries between the body of jets and external medium. Body waves propagate through the body of a fluid or only exist in the interior of the medium, such as acoustic/magnetosonic waves. The existence of body waves does not depend on the presence of boundaries, but the reflection and/or refraction of body waves by such boundaries leads to the growth of modes that could eventually cause the disruption of jets (Zhao et al. 1992a; Hardee, Clarke, & Rosen 1997).

Beginning with the pioneering work by M. L. Norman and his co-investigators (Norman et al. 1982), numerical simulations have been performed to investigate the nonlinear development of KH instabilities for propagating jets (Kössl & Müller 1988; Cioffi & Blondin 1992; Massaglia, Bodo, & Ferrari 1996; Carvalho & O’Dea 2002a,b; Krause 2003). Norman et al. (1982) performed the axisymmetric 2-D HD simulations and found that the jet is decelerated by a Mach-disc shock wave front that is, in general, much stronger than the bow shock of the jet. Backflow from the working surface builds an extensive cocoon or lobe surrounding the jet. Hypersonic jet flow itself is largely stable to KH instabilities, which grow slowly compared to the jet propagation speed. The transonic lobes and cocoons, however, are generally KH *unstable* and mix with the external gas at a ragged boundary.

Another type of numerical approach investigates the nonlinear development of KH instabilities in pre-formed “*equilibrium*” jets which begin in radial force equilibrium. A thermally confined top-hat velocity profiled jet, surrounded by a uniform unmagnetized external medium, was investigated with both 2-D (Norman & Hardee 1988; Zhao et al. 1992b; Bodo et al. 1994, 1995; Stone, Xu, & Hardee 1997) and 3-D simulations (Hardee & Clarke 1992; Bodo et al. 1998; Xu,

Hardee, & Stone 2000; Micono et al. 2000). These jets are perturbed at the surface layer between jet flow and external medium, and axisymmetric and non-axisymmetric surface and body modes of KH instabilities sometimes grow under a variety of conditions.

## 2.4. Stability of MHD Jets

### 2.4.1. Kelvin-Helmholtz instabilities

The MHD KH instability of jets has been examined using linear stability analysis (Ray 1981; Ferrari, Trussoni, & Zaninetti 1981; Cohn 1983; Fiedler & Jones 1984; Bodo et al. 1989; Hardee et al. 1992; Bodo et al. 1996). In general, surface non-axisymmetric modes ( $m > 0$ ) are stable against MHD KH instability during sub-Alfvénic flow. However, in super-Alfvénic but trans-fast magnetosonic flow, they can be unstable. The surface symmetric mode ( $m = 0$ ) is predicted to be MHD KH unstable in sub-Alfvénic and super-Alfvénic flow, although with a relatively small growth rate (Bodo et al. 1989; Hardee et al. 1992; Hardee, Clarke, & Rosen 1997). However, body mode waves can become important and affect the jet interior in the following situations: (1) if jet velocity exceeds the super-fast magnetosonic speed ( $V_{FM} < V_j$ ) or (2) if the flow velocity is slightly below the slow magnetosonic speed [ $C_s V_A / (C_s^2 + V_A^2)^{1/2} < V_j < V_{SM}$ ] (Hardee & Rosen 1999).

The growth of KH instabilities of super-fast magnetosonic jets containing force-free helical magnetic field has been shown to be reduced by the presence of a toroidal magnetic field (Appl & Camenzind 1992). Similar investigations extended to the sub-fast magnetosonic regime (Appl 1996) showed that the toroidal field exhibits a *destabilizing* behavior at small velocities. At least for force-free helical magnetic configurations in linear regime, it appears that the KH mode exhibits faster growth than CD mode (Appl 1996). Bodo et al. (1996) investigated the axially magnetized rotating super-fast magnetosonic jets, and they found that these jets could be stabilized against the non-axisymmetric surface mode by jet rotation. If there exists an external wind between the jet and the ambient medium, these results are modified considerably.

Clarke, Norman, & Burns (1986), Lind et al. (1989), and Krause & Camenzind (2001) performed axisymmetric 2-D simulations of propagating MHD jets with a purely toroidal magnetic field and an unmagnetized external medium. Kössl, Müller, & Hillebrandt (1990) investigated the MHD jets with a helical (poloidal + toroidal) magnetic field (with the external medium poloidally magnetized) using axisymmetric 2-D simulations. The results of these investigations showed that a strong toroidal magnetic field makes the backflow weak in the cocoon and, consequently, reduces the growth rate of the KH instabilities. Todo et al. (1992) also performed axisymmetric 2-D simulations of MHD jets assuming a force-free helical magnetized external medium with

the injection of super-Alfvénic flows into the computational domain. In their investigation, the KH instability is entirely suppressed if the the magnetic field is parallel to the velocity shear between cocoon and shroud and if the following criterion is satisfied (*e.g.*, Chandrasekhar 1961):  $\rho_1\rho_2(V_1 - V_2)^2 \leq (\rho_1 - \rho_2)B^2/8\pi$ . Here  $\rho$ ,  $V$ , and  $B$  are the density, velocity, and magnetic field strength parallel to the velocity, respectively, with subscripts denoting the two different fluids. For the present case, subscript 1 corresponds to the cocoon and 2 represents the shroud. Todo et al. (1992) derived a qualitative tendency in which the dense external medium ( $\rho_1/\rho_2 \lesssim 0.1$ ) promotes the KH instability, whereas the large scale magnetic field suppresses it.

Recently, using 3-D simulations, Ouyed, Clarke, & Pudritz (2003) investigated the ejection and propagation of a MHD jet from a pseudo-Keplerian disk (*i.e.*, the disk is treated as a fixed boundary condition which has a Keplerian-like azimuthal velocity profile, but does not allow accretion) (see *e.g.*, Bell & Lucek 1995; Ustyugova et al. 1995; Meier et al. 1997; Ouyed & Pudritz 1997a,b, 1999). Their results showed that the MHD jet beyond the Alfvén surface temporarily becomes unstable to the non-axisymmetric ( $m > 0$ ) KH instability. However, the jet maintains long-term stability via a self-limiting process that keeps the average Alfvén Mach number within the jet to of order unity. This occurs because the poloidal magnetic field becomes concentrated along the central axis of the jet, forming a “backbone” in which the Alfvén speed is high enough to reduce the average jet Alfvénic Mach number to unity.

Of particular interest are the axially magnetized 2-D slab equilibrium jets (Hardee et al. 1992; Hardee & Clarke 1995) and the helically magnetized 3-D equilibrium cylindrical jets investigated by P. E. Hardee and his collaborators (Hardee, Clarke, & Rosen 1997). In the super-Alfvénic regime, if the jet is *also* super-fast magnetosonic, then it becomes more stable with increasing fast magnetosonic Mach number ( $M_{\text{FM}}$ ), and the destabilization length ( $L$ ) varies approximately proportional to  $M_{\text{FM}}$  ( $L \propto M_{\text{FM}}R_j$ , where  $R_j$  is the jet radius). Hardee & Rosen (1999) investigated helically magnetized 3-D trans-Alfvénic “light” jets (density ratio  $\rho_j/\rho_e \sim 0.03$ , where subscript “j” corresponds to the jet itself and “e” corresponds to the external medium). These experienced considerable slowing as denser material was entrained following destabilization; provided the jet is super-Alfvénic, their KH growth rates also increase as  $M_{\text{FM}}$  decreases. However, the jets are nearly completely stabilized to these instabilities when the jet is sub-Alfvénic.

These numerical results show that the super-Alfvénic but trans-fast magnetosonic flow region is a potential zone of enhanced KH instabilities just downstream of the Alfvén point. They also show that magnetic tension can significantly modify the development of the KH instability in non-linear regime. An increase of density ratio would stabilized the MHD jets beyond the Alfvén point and, in general, denser jets have been found to be more robust than their less dense counterparts (Rosen et al. 1999; Rosen & Hardee 2000). Hardee & Rosen (2002) confirmed the stabilizing influence of a surrounding magnetized wind against the non-axisymmetric KH surface modes of

the helically magnetized 3-D trans-Alfvénic jets. They concluded that the jets could be stabilized entirely to the non-axisymmetric KH surface modes if the velocity shear,  $\Delta V \equiv V_j - V_e$  is less than a “surface” Alfvén speed,  $V_{As} \equiv [(\rho_j + \rho_e)(B_j^2 B_e^2)/(4\pi\rho_j\rho_e)]^{1/2}$ .

#### 2.4.2. Current-driven instabilities

Prior to this point in time, much less consideration has been given to CD instabilities than to KH instabilities in the investigation of the disruption of the interior of astrophysical jets. This has been because, until recently, jets were believed to be in super-Alfvénic or super-fast magnetosonic flow (*i.e.*, kinetic energy was expected to exceed magnetic energy). Some analytic studies on CD instabilities as a possible explanation for jet disruption had been done (Eichler 1993; Spruit, Foglizzo, & Stehle 1997; Begelman 1998; Lyubarskii 1999). Appl, Lery, & Baty (2000) also analyzed, for a large range of magnetic pitch ( $rB_z/B_\phi$ ), the CD linear growth rate for configurations with a force-free helical magnetic field and a constant distribution of density and velocity. (These assumptions exclude PD and KH instabilities.) They concluded that the properties of the fastest growing CD kink ( $m = 1$ ) mode are nearly independent of the details of the pitch profile. However, they also concluded that this was an internal mode that does not cause a significant distortion of jet.

Lery, Baty, & Appl (2000) studied the nonlinear development of CD instability for cold super-fast magnetosonic equilibrium jets based on their linear analysis (Appl, Lery, & Baty 2000). It was found that the current density is redistributed within the inner part of the jet radius on a characteristic time scale of order the Alfvén crossing time in the jet frame. Nothing in their numerical results indicated a possible disruption of jet by the CD sausage ( $m = 0$ ) or kink ( $m = 1$ ) mode. However, for numerical reasons, their simulations were limited to early nonlinear phases; a full investigation of the nonlinear development of the instability was not carried out.

Todo et al. (1993) performed 3-D MHD simulations of a model for HH objects in which super-Alfvénic propagating jets are injected into a pre-formed force-free helically magnetized ambient medium. They found that YSO jets can be disrupted into a large scale wiggled structure by the CD kink instability. In a similar study, Nakamura, Uchida, & Hirose (2001) performed 3-D simulations of propagating MHD jets to investigate the formation of wiggled structures in AGN jets. They found that the propagation of nonlinear torsional Alfvén waves (TAWs) can produce a slender jet shape by the “sweeping magnetic twist” mechanism of Uchida & Shibata (Shibata & Uchida 1985, 1986; Uchida & Shibata 1985, 1986). In addition, wiggles in the jet can be produced by the CD kink instability though the interaction between the TAW and the ambient medium. Recently, Baty & Keppens (2002) confirmed the interaction of KH and CD instabilities in helically magnetized super-fast magnetosonic equilibrium jets by performing 3-D MHD simulations.

This nonlinear interaction can contribute to jet survival, and the large-scale magnetic deformations associated with CD mode development can effectively saturate KH surface vortices and prevent jet disruption.

## 2.5. Theoretical Arguments for Poynting Flux Dominated Jets

There has been a growing recognition in recent years that Poynting flux dominated (PFD) flow plays an important role in the jets in AGNs, QSOs, winds from pulsars, and possibly  $\gamma$ -ray burst sources. This is in strong contrast to the kinetic energy flux dominated (KFD) jets that had been expected in these sources, and still are believed to be relevant for YSO jets. The energy carrier of PFD jets is primarily the electromagnetic field, while in KFD jets it is the kinetic flux.

The concept of PFD jets is based on the theory of magnetically driven outflow, proposed (in the electromagnetic regime) by Blandford (1976) and Lovelace (1976) and subsequently applied to rotating black holes (Blandford & Znajek 1977) and to magnetized accretion disks (Blandford & Payne 1982). By definition, these outflows initially are dominated by electromagnetic forces close to the central engine. In these and subsequent models of magnetically driven outflows (jets/winds), the plasma velocity passes successively through the hydrodynamic (HD) sonic, slow-magnetosonic, Alfvénic, and fast-magnetosonic critical points (surfaces). In very strongly magnetized flows ( $C_s \ll V_A$ ), the hydrodynamic and slow-magnetosonic points almost coincide, and the Alfvén and fast points also occur close to each other. The distance between these two clusters of critical points (HD/slow and Alfvén/fast), and therefore the nature of much of the outflow, depends on the relative dominance of the advected magnetic field, *i.e.*, on how long the high level of Poynting flux domination can be maintained as the flow propagates.

In many early models of steady, axisymmetric MHD outflow, it was expected that the flow would smoothly pass the Alfvénic point (surface) at a distance very close to the central object. After that the flow would become super-Alfvénic and, therefore, kinetic energy flux dominated. However, according to recent theoretical studies, this picture is probably not correct. Of particular interest here is the current-carrying core of the outflow near the central axis (the jet). In steady non-relativistic solutions (Fendt & Camenzind 1996; Krasnopolsky, Li, & Blandford 1999) the innermost part of the outflow remains sub- to trans-Alfvénic ( $M_A \lesssim 1$ ), *i.e.*, Poynting flux dominated. Furthermore, in relativistic steady models of MHD outflows from disks, the flow can remain PFD for many hundreds to thousands of outer disk radii — tens of parsecs in AGN (Vlahakis & Königl 2001, 2003a,b, 2004). Even in dynamical simulations, a self-organized process occurs whereby the Alfvén speed increases due to the concentration of poloidal magnetic flux  $\mathbf{B}_p$  along the central axis of the outflow (Ouyed, Clarke, & Pudritz 2003). This reduces  $M_A$  near the axis and forestalls the passage of the flow through the Alfvén point.

So, it appears likely that the axial part of the outflow (the current-carrying jet) remains in sub-trans-Alfvénically PFD flow for a long distance. In the case of AGN jets this translates into a few to several tens of parsecs. *Jets observed by VLBI, therefore, may be Poynting flux dominated, making our simulations herein directly applicable.*

Further theoretical development of PFD jets from magnetized accretion disks has been performed by Begelman, Blandford, & Rees (1984); Lovelace, Wang, & Sulkanen (1987); Li, Begelman, & Chiueh (1992); Lynden-Bell (1996); Romanova & Lovelace (1997); Levinson (1998); Colgate & Li (1999); Li et al. (2001); Lovelace et al. (2002); Heyvaerts & Norman (2003a,b,c); Lovelace & Romanova (2003); and Vlahakis (2003). Two-dimensional axisymmetric (“2.5-D”) non-relativistic MHD simulations of PFD jets have been performed for opening magnetic loops threading a Keplerian disk (Romanova et al. 1998; Ustyugova et al. 2000). And relativistic 2.5-D simulations of propagating PFD jets carrying a toroidal field component only were performed by Komissarov (1999) in order to compare their simulations with the non-relativistic simulations of Lind et al. (1989). Finally, Li (2000), Tomimatsu, Matsuoka, & Takahashi (2001), and Wang et al. (2004) have considered analytically the CD instability (the so-called “screw instability”) of black hole magnetospheres.

To our knowledge, however, no study has been made of the nonlinear behavior of PFD jets and the related CD instabilities in full 3-D dynamics.

### 3. NUMERICAL METHODS

#### 3.1. Basic Astrophysical Model

In this paper we study the structure, dynamics, and stability of propagating MHD jets. Our simulations concentrate on the region in an AGN in which a collimated jet-like flow (at much greater than the escape velocity) has been established, but that flow still is dominated by magnetic forces and has not yet achieved a super-(fast magneto) sonic velocity. The energy carried by the jet, therefore, is dominated by Poynting flux rather than kinetic energy flux, and the Alfvén speed in the flow is much higher than the local sound speed,  $C_s \ll V_A$ .

Numerous theoretical investigations of the central engine itself have shown that a rotating, magnetic structure can be created a few Schwarzschild radii ( $10^{14-15}$  cm) from the black hole (Blandford & Znajek 1977; Blandford & Payne 1982; Koide et al. 2002). While the physical connection between this central region and the sub-parsec region is still poorly understood, it is reasonable to suppose that both strong magnetic and rotational fields will be influential at the base of the sub-parsec flow. Our basic jet model, therefore, contains a plasma with a strong, rotating poloidal magnetic field at its base. Nonlinear TAWs propagate out along this field, creating and

propagating a magnetically driven collimated outflow via the sweeping magnetic twist mechanism of Uchida & Shibata (1986).

In contrast with the many numerical stabilities studies, in which the magnetized jets are assumed to be confined thermally by a non-magnetized external ambient medium, we assume a large scale poloidal magnetic field in the ambient medium surrounding the jet. The origin of such a galactic magnetic field is not yet fully understood, but its existence is suggested by both synchrotron emission and Faraday rotation observations. The magnetic field assumed here might either be a part of the primordial inter-stellar field (Kulsrud & Andersen 1992) brought into the central part of the protogalaxy in the process, or the central part of the amplified field by a galactic turbulent dynamo process, which are argued by many authors (for reviews, see Kronberg 1994; Han & Wielebinski 2002, and references therein), or a field structure carried out from the central engine by a lower-velocity magnetized disk wind.

Models of the central parsec and sub-parsec regions of galaxies indicate that the ambient medium is characterized by strongly decreasing gradients in density and pressure and, presumably, magnetic field. We therefore are especially interested in the behavior of PFD jets in decreasing density atmospheres.

### 3.2. MHD Equations and Simulation Code

In the present study we assume non-relativistic ideal MHD and neglect the effect of gravity. We solve the nonlinear system of time-dependent MHD equations numerically in 3-D Cartesian coordinate system  $(x, y, z)$ :

$$\frac{\partial \rho}{\partial t} + \nabla \cdot (\rho \mathbf{V}) = 0, \quad (1)$$

$$\rho \left[ \frac{\partial \mathbf{V}}{\partial t} + (\mathbf{V} \cdot \nabla) \mathbf{V} \right] = -\nabla p + \mathbf{J} \times \mathbf{B}, \quad (2)$$

$$\frac{\partial \mathbf{B}}{\partial t} = \nabla \times (\mathbf{V} \times \mathbf{B}), \quad (3)$$

$$\frac{\partial p}{\partial t} + \nabla \cdot (p \mathbf{V}) = -(\Gamma - 1)p \nabla \cdot \mathbf{V}. \quad (4)$$

Here,  $\rho$  is the mass density,  $p$  the gas pressure,  $\mathbf{V}$  the fluid velocity.  $\mathbf{B}$  is the magnetic field and  $\mathbf{J} = (\nabla \times \mathbf{B})/4\pi$  is the corresponding current density.  $\Gamma$  is the ratio of specific heats (a value of 5/3 is used).

We normalize all physical quantities with the unit length scale  $L_0$ , typical density  $\rho_0$ , typical velocity  $V_0$  in the system, and their combinations, *e.g.*,  $\rho' = \rho/\rho_0$ , etc. The normalizing factors are

shown in Table 1. A factor of  $4\pi$  has been absorbed into the scaling for both the magnetic field  $\mathbf{B}$  and the current density  $\mathbf{J}$ . This normalization does not change the form of the basic equations (1) – (4), and hereafter, we will use the normalized variables and will omit the primes on physical quantities. (We will write the dimensional variables with subscript "0":  $\rho_0$ , for example.) The system of dimensionless equations is integrated in time by using a two-step Lax-Wendroff scheme (Rubin & Burstein 1967) with artificial viscosity term (Lapidus 1967). The original MHD code was developed by K. Shibata and extended by his co-workers (*e.g.*, Shibata 1983; Shibata & Uchida 1985, 1986; Matsumoto et al. 1996). Parallelization of the code was done using MPI.

The total computational domain is taken to be  $|x| \leq x_{\max}$ ,  $|y| \leq y_{\max}$ , and  $z_{\min} \leq z \leq z_{\max}$ , where  $x_{\max}$ ,  $y_{\max} \simeq 16.0$ ,  $z_{\min} \simeq -1.0$ , and  $z_{\max} \simeq 20.0$ . The numbers of grid points in the simulations reported here are  $N_x \times N_y \times N_z = 261 \times 261 \times 729$ , where the grid points are distributed non-uniformly in the  $x$ ,  $y$ , and  $z$  directions. The grid spacing in the initial propagation region near the jet axis is uniform,  $\Delta x = \Delta y = \Delta z = 0.025$  for  $|x|$ ,  $|y| \leq 1.5$  and  $|z| \leq 16.0$  ( $121 \times 121 \times 681$  cells are assigned here), and then stretched by 5% per each grid step for the regions  $|x|$ ,  $|y| > 1.5$  and  $|z| > 16.0$ . Forty uniform cells are distributed across the initial jet diameter in the transverse direction,  $L \simeq 1$  at  $z = 0$ . Low-resolution exploratory computations were performed on the Jet Propulsion Laboratory Origin 2000 machines. High-resolution 3-D computations were performed on the FUJITSU VPP 5000/32R at the National Astronomical Observatory in Japan (9.6 GFLOP/s peak speed per node) requiring about 6 CPU hours each.

### 3.3. Initial Conditions: Non-uniform magnetized atmospheres

In the non-uniform, magnetized atmosphere we adopt a current- (and therefore force-) free magnetic configuration ( $\mathbf{J} = 0$ ), by placing one pair of current loops on both the upper and lower  $z$ -boundaries of the computational domain. This constrains the magnetic field to have only a field  $z$ -component at  $z = z_{\max}$ , thereby avoiding numerical errors when physical MHD waves pass through the upper ( $z = z_{\max}$ ) boundary. Such a field configuration does not disturb the force equilibrium of the hydrostatically stable atmosphere because  $\mathbf{J} \times \mathbf{B} = 0$ . The field configuration chosen is explicitly given in the Appendix.

For our initial density distribution, we assume that  $\rho$  varies as a power of the magnetic field strength

$$\rho \propto |\mathbf{B}|^\alpha, \quad (5)$$

where  $\alpha$  is a free parameter in this paper. If  $\alpha = 2$ , the Alfvén speed  $V_A (\equiv |\mathbf{B}|/\sqrt{\rho})$  will be constant throughout the computational domain. If  $\alpha \neq 2$ , the Alfvén speed will decrease ( $\alpha < 2$ ) or increase ( $\alpha > 2$ ) with distance from origin (0, 0, 0). This power law model embraces several accretion and

collapse models for the formation of the interstellar medium (ISM).

- For example, if the ISM had formed by the conservative spherical contraction of a protogalactic gas cloud, the magnetic field strength  $|\mathbf{B}|$  would be amplified as  $|\mathbf{B}| \propto \rho^{2/3}$  or  $\alpha = 3/2$ . Combining this value for  $\alpha$  with our initial magnetic field distribution, the polar (axial) distribution of Alfvén velocity  $V_{Az}(z) (\equiv B_z/\sqrt{\rho})$  would gradually decrease as  $V_{Az}(z) \propto z^{-1/2}$  [ $B_z(z) \propto z^{-2}$ ,  $\rho(z) \propto z^{-3}$ ].
- In the case of interstellar magnetized clouds (isothermal gravitational contractions),  $2 \leq \alpha \leq 3$  is theoretically (Mouschovias 1976), numerically (Scott & Black 1980), and observationally inferred (Crutcher 1999) rather than  $\alpha = 3/2$ . However,  $\alpha$  varies widely with position  $(r, z)$  in the contracting gas, and is smaller than 2 near the central  $(z)$  axis, because the field there is being “dragged along” by the collapse in the  $r$ -direction. This leads to a large amplification of the field with no corresponding large increase in  $\rho$ ; thus  $\alpha$  becomes small (Mouschovias 1976; Scott & Black 1980).  $\alpha \sim 2$  [ $\rho(r) \propto B_z(r)^2$ ] on the equatorial plane and  $\alpha \sim 1$  [ $\rho(z) \propto B_z(z)$ ] on the central axis of collapsing gas, also have been found with numerical simulations (Tomisaka 1996).
- A third possibility is that the ISM may have formed in an advection-dominated accretion flow (Narayan, Mahadevan, & Quataert 1998), where  $\rho \propto r^{-3/2}$  and  $|\mathbf{B}| \propto r^{-5/4}$ , or  $\alpha = 6/5$ .

We therefore choose the following two representative cases: “*decreasing*  $V_A$ ” ( $\alpha = 1$ ) and “*constant*  $V_A$ ” ( $\alpha = 2$ ) as the initial ambient medium.

For the initial gas pressure distribution we make the polytropic assumption

$$p \propto \rho^\Gamma, \quad (6)$$

where  $\Gamma$  is the polytropic index (we use  $\Gamma = 5/3$  throughout this paper). The sound speed  $C_s$  ( $\equiv \sqrt{\Gamma p/\rho} \propto T^{1/2}$ , with  $T$  being the temperature) will decrease with distance from origin. The atmosphere is artificially confined to prevent it from expanding under its own pressure gradient by imposing a pseudo-gravitational potential ( $\tilde{\phi}$ ) designed to ‘hold on to’ the atmosphere without significantly impeding the advancing jet (Clarke, Harris, & Carilli 1997):

$$\tilde{\phi} \equiv \frac{\tilde{p}}{\tilde{\rho}}. \quad (7)$$

Here,  $\tilde{p}$  and  $\tilde{\rho}$  are the initial gas pressure and density distributions. By design, the quantity  $\rho\tilde{\phi}$  exactly cancels the initial gas pressure gradients in the stratified atmosphere,  $\nabla(p - \rho\tilde{\phi}) = 0$ . Assuming a current-free ( $\mathbf{J} = 0$ ) field, the right-hand side of equation (2) exactly equals zero.

We now consider the “plasma- $\beta$ ” parameter:

$$\beta \equiv \frac{2p}{|\mathbf{B}|^2} = \frac{2C_s^2}{\Gamma V_A^2} \quad (8)$$

as the ratio of the gas to the magnetic pressure. In all the situations we investigate in this paper, the thermal energy density is much less than the magnetic energy density, so  $\beta \sim C_s^2/V_A^2 \ll 1$  in the whole computational domain.

### 3.4. Boundary Conditions

In the lower “boundary zone” [ $z_{\min} \leq z < 0$ , where  $r = (x^2 + y^2)^{1/2}$ ] we set the velocity field to be

$$\mathbf{V}_j = V_\phi(r, z)\hat{\phi} + V_z(r, z)\hat{z}. \quad (9)$$

This zone is the injection region, in which the hypersonic but sub-Alfvénic flow (*i.e.*, the PFD jet) is formed. Equation (9) represents a cylindrical MHD jet, powered by a nonlinear TAW, entering the upper region ( $z \geq 0$ ) of the computational domain. In all our simulations the injection speed of the PFD jet in the boundary zone is sub-Alfvénic, but super-slow magnetosonic.

To stabilize the numerical calculations in the injection region, we employed a “damping zone” to prevent unnecessary reflections and interactions from below. The disturbances in all physical quantities except for the magnetic field are damped at each time steps as follows:

$$Q(x, y, z, t) = \{1 - f_Q(z)\} Q(x, y, z, t) + f_Q(z) Q(x, y, z, 0), \quad (10)$$

$$f_Q(z) \equiv \frac{1}{2} \left\{ \cos \left( \frac{z - z_1}{z_2 - z_1} \pi \right) + 1 \right\}. \quad (11)$$

The damping factor  $f_Q$  for quantity  $Q$  is defined such that it is equal to zero at the upper end of the damping zone,  $z \geq z_2$ , and to unity at the lower end,  $z \leq z_1$ . We set the values to  $z_1 = -0.975$  and  $z_2 = -0.025$ , respectively. We use about 40 axial cells in this boundary zone. Note that we leave the magnetic field  $\mathbf{B}(x, y, z, t)$  unmodified so that the induction equation (3) still holds.

At the bottom of this zone ( $z = z_{\min}$ ), we impose symmetry for  $\rho$ ,  $V_x$ ,  $V_y$ ,  $B_z$ , and  $p$ , and antisymmetry for  $V_z$ ,  $B_x$ ,  $B_y$ . The free time-dependent evolution of the flow physical variables occurs only in the upper part of the computational domain ( $z \geq 0$ ).

At the outer boundaries ( $x = x_{\min}$ ,  $x = x_{\max}$ ,  $y = y_{\min}$ ,  $y = y_{\max}$ , and  $z = z_{\max}$ ) we set free conditions for each quantity  $Q$  as follows Shibata (1983):

$$\frac{\partial \Delta Q}{\partial x} = \frac{\partial \Delta Q}{\partial y} = \frac{\partial \Delta Q}{\partial z} = 0,$$

$$\Delta Q \equiv Q(x, y, z, t + \Delta t) - Q(x, y, z, t). \quad (12)$$

## 4. RESULTS AND DISCUSSION

In this section we provide a detailed description of the evolution of four different simulations of PFD jets. We will concentrate on the solutions in the “jet-propagation” region,  $-2.25 \leq x, y \leq 2.25$ , and  $0.0 \leq z \leq 18.0$ . An important unit time scale in these dimensionless systems is the Alfvén crossing time  $\tau_A$  ( $\equiv L/V_A$ ), normalized with  $\tau_{A0} \equiv L_0/V_{A0}$ .

### 4.1. The Four Initial Models

We have carried out a number of simulations with varying physical conditions, evolving four distinct models: shallow-atmosphere models (A) and steep-atmosphere models (B), each with a highly and a mildly Poynting flux dominated flow case. The values of their physical parameters listed in Table 2 and discussed more fully below.

The main purpose of this investigation is to study the effects of a decreasing density, magnetized ambient medium on the growth of current-driven instabilities in dynamically propagating PFD jets. Figure 1 shows the initial ( $t = 0.0$ ) distribution of the physical quantities along the  $z$ -axis. For the A models ( $\alpha = 1$ ; *decreasing*  $V_A$ ),  $\rho$  and  $B_z$  decrease gradually along the  $z$ -axis and asymptote to  $\sim z^{-2}$  for  $z > 1$ . On the other hand, for the B models,  $B_z$  decreases in the same manner as model A, but  $\rho$  decreases faster than  $\sim z^{-2}$  for large  $z$  ( $\alpha = 2$ ; *constant*  $V_A$ ). We set the plasma beta ( $\beta = 10^{-2}$ ) at the origin for all of the models. The ratio  $V_A/C_s$  decreases slightly along  $z$ -axis for model A but gradually increases for model B.

We also consider two different types of flow in each atmosphere model, *i.e.* the ratio of Poynting flux  $F_{E \times B}$  to the total energy flux  $F_{\text{tot}}$  in MHD jets:

1. Highly PFD jets ( $F_{E \times B}/F_{\text{tot}} \sim 0.9$ ) (Case 1)
2. Mildly PFD jets ( $F_{E \times B}/F_{\text{tot}} \sim 0.6$ ) (Case 2)

Figure 2 shows the time variation of the ratio of the injected energy fluxes into the upper “evolved region” from the lower boundary zone. Note that the quasi-stationary PFD flow is injected through the time evolution of the system. The net amount of injected *Poynting flux* for the mildly PFD jets is almost equal to the case of the highly PFD jets. However, the amount of *kinetic energy flux* injected in Case 2 is considerably larger than in Case 1.

## 4.2. Comparative Overview of Simulation Evolution

Before considering our numerical results in detail, it is instructive to give a brief comparative overview of the time development of the jet systems in the four models. This can be done by inspecting the logarithmic density  $\rho$  and the velocity field  $(V_x, V_z)$  normalized by  $V_{A0}$ . Figures 3 – 6 display these quantities at various times in the simulation evolution using two-dimensional  $x - z$  slices at  $y = 0$ . Note that these slices contain the jet ( $z$ ) axis.

### 4.2.1. Early jet evolution: propagation of the nonlinear MHD waves

At early times in the evolution (*Top* part of each Figs. 3–6), the well-collimated helically PFD jets powered by the TAWs advance into the poloidally magnetized ambient medium. Figure 7 displays for all models the axial distributions of the Alfvén and sound speeds, as well as each component of the jet velocity, in the  $x - z$  plane close to the jet axis. The propagation of three distinct fronts of compressive MHD waves is clearly visible for all models: a fast-mode MHD wave (at the head of the PFD jet or TAW) and a pair of slow-mode MHD waves further upstream. We characterize these waves as propagating in both the forward (F) and reverse (R) directions relative to a reference frame that co-moves with the jet, and give them the names forward fast-mode (F–F), forward slow-mode (F–S), and reverse slow-mode (R–S) waves. In addition, a contact discontinuity travels in this co-moving frame between the two slow-mode waves. Because the jet is injected at a super-slow magnetosonic velocity in the boundary zone, the forward and backward (reverse) propagating slow-mode compressive waves seen in each of the models quickly become slow-mode shock waves early in the simulation.

In models A – 1 and A – 2, due to a gradual decreasing ambient  $V_A$ , the F–F compressive wave front decelerates and its wave amplitude gradually increases as it propagates forward. Through this nonlinear process, this front steepens into a *fast-mode MHD bow shock* when the phase velocity becomes super-fast magnetosonic (see also the *2nd* panels in Fig. 3 and 4).

On the other hand, only a very low amplitude F–F compressive wave front can be (barely) seen in models B – 1 and B – 2 in Figure 7. This wave front never reaches a super-fast magnetosonic velocity during our simulations of models B. The velocity amplitude associated with the F–F compressive wave becomes much weaker as the ratio  $V_A/C_s$  in the ambient medium [ $\equiv (2/\Gamma\beta)^{1/2}$ ] along  $z$ -axis increases. The phase velocity of a fast-mode compressive MHD wave is  $V_{\text{ph}} = V_{\text{FM}} \sim V_A$  when  $C_s^2 \ll V_A^2$ . Because the initial distribution of the Alfvén velocity in Models B – 1 and B – 2 is constant with  $z$  ( $V_A = 1.0$ ), the F–F compressive wave will propagate quickly compared with models A – 1 and A – 2. In the B models the wave reaches  $z = 18.0$  at a time  $t \sim 18.0$ .

Several features of PFD MHD jet flow have counterparts in the well-known supersonic hydro-

dynamic jet flow. The F–F compressive/shock wave, of course, propagates through the external medium at a speed faster than the other two shock waves, playing the same role as the bow shock does in HD jets. The F–S shock wave propagates at a slower speed, further compressing and heating the ambient medium. This second shock wave has no direct counterpart in HD jets, although it acts similarly to the bow shock, especially when the F–F front is a compressive wave. The reverse (R–S) shock wave plays the same role as the Mach disk does in HD jets, decelerating and heating the magnetized jet flow itself. From the point of view of the jet material, the flow can reach the R–S shock wave and enter the compressed region, but it can never reach the F–S shock wave. Similarly, the external ambient material crossing the F–S shock wave also reaches this heated region, but can never reach the R–S shock wave. Instead, ambient material is entrained between the two slow-mode shock waves, along with the accumulated jet material. The contact discontinuity between the two accumulations, therefore, plays the same role as the contact discontinuity in HD jets. We often identify this interface as defining the rest frame of the jet flow.

#### 4.2.2. *Intermediate jet evolution: energy conversion through the MHD shocks*

In the “intermediate stages” of the flow (2nd panel each in Figs. 3–6), the gas is weakly compressed in the  $z$  direction across the first (F–F) compressive/shock wave, and then is strongly compressed further across the second (F–S) shock wave. In addition, the gas crossing the third (R–S) shock wave also is expanded by a large ratio, but in the opposite direction. Because the greatest compression occurs when the gas crosses the slow shock waves, the material undergoes extensive heating and accumulates in the region between these two wave fronts. In the shallow-atmosphere models A the structure of the pair of slow shock waves does not change during the simulation. However, in models B this structure undergoes an expansion in the transverse direction because of the steeply decreasing gradient in the external ambient pressure.

Figures 8 and 9 show snapshots of  $V_y$  and  $B_y$  (similar to Fig. 3 – 6) at the time when the head of the PFD jet reaches  $z = 10.0$  in each of the models. ( $V_y$  and  $B_y$  correspond to  $V_\phi$  and  $B_\phi$  in cylindrical coordinates.) Below the flow through each compressive/shock wave is described in the shock frame (in the negative  $z$  direction for the F–F and F–S shock waves and in the positive  $z$  direction for the R–S shock wave). We now can compare the energy conversion in each of Figs. 8 and 9:

1. The toroidal component of the magnetic field ( $B_y$ ) increases strongly as the flow crosses the F–F shock wave front (in the  $-z$  direction; models A – 1 and A – 2). However, that component increases only weakly across the F–F compressive wave (models B – 1 and B – 2). Therefore, *the toroidal (rotational) kinetic energy of a PFD jet is strongly converted into toroidal magnetic energy across the F–F shock wave in the shallow-atmosphere models A,*

*but not so much in the steep-atmosphere models B.*

2. The toroidal component of the magnetic field *decreases* across the F–S shock wave, and the toroidal component of the velocity field also decreases across it. Therefore, *the toroidal kinetic and magnetic energy of a PFD jet are converted into thermal and axial kinetic energy across the F–S shock wave.*
3. The toroidal component of the magnetic field also decreases as the flow crosses the R–S shock wave (in the  $+z$  direction). However, unlike the first slow-mode shock wave, the toroidal component of the velocity field does *not* decrease across the second. It actually *increases* as material flows into the region between the two slow-mode shock waves. (Note the relative strength of the toroidal component of the velocity beyond the F–S shock wave and behind the R–S shock wave in the frame co-moving with the contact discontinuity for Case A – 2 in Fig. 8.) Therefore, *axial kinetic and toroidal magnetic energy are converted into thermal and toroidal kinetic energy across the R–S shock wave.*<sup>1</sup>

So, we expect that the magnetic field between the second and the third shock waves will be less twisted, whereas that between the first and second, and behind the third, shock waves will be more twisted. This physical picture is similar to the results of 1.5-dimensional MHD simulations performed by Uchida et al. (1992).

#### 4.2.3. Nature of PFD jets as current-carrying jets

We now consider the behavior of PFD jets as current-carrying systems. Figure 10 shows snapshots of the axial current density  $J_z$  (similar to Fig. 8 and 9) at the time when the head of the PFD jet reaches  $z = 10.0$  in each models. Clearly, the flow displays a closed circulating current system, in which one path occurs close to the central axis, and co-moves with the PFD jet (the “forward jet current density”  $\mathbf{J}^{jc}$ ) and another conically-shaped path that flows outside (the “return current density”  $\mathbf{J}^{rc}$ ).

---

<sup>1</sup>At first it would appear that the behavior of two slow-mode shock waves is strangely asymmetric. However, if one transforms to the translating *and rotating* frame of the contact discontinuity between these two shock waves, one finds that the behavior of all energy components (axial and toroidal kinetic, toroidal magnetic, and thermal) are all precisely symmetric. In particular, at both slow-mode shock waves toroidal kinetic energy *decreases* in this frame, and is converted into thermal energy, as the flow crosses into the region between them. There is only one real asymmetry: the change in the sense of rotation across the two slow-mode shock waves is *anti*-symmetric. This antisymmetry is caused by the axial speeds of the two shock waves being opposite in this frame while the handedness of the magnetic field pitch, and therefore  $V_\phi$ , is the same.

Figure 11 shows (at the same times as in Fig. 10) the transverse profile of the force-free parameter  $\lambda_{\text{ff}} (\equiv \mathbf{J} \cdot \mathbf{B} / |\mathbf{J}| |\mathbf{B}|)$  and the axial current density  $J_z$  near the lower ( $z = 2.2$ ) and upper ( $z = 8.3$ ) regions. The diagram shows that the jets relax into radial force balance with the ambient medium: there is a current-carrying core  $\mathbf{J}^{\text{jc}}$  in the jet itself and a return-current skin  $\mathbf{J}^{\text{rc}}$  outside, both of which are in approximate force-free equilibrium ( $\mathbf{J} \times \mathbf{B} \simeq 0$ ). (The reversal of sign from  $\lambda_{\text{ff}} = -1$  to 1 indicates a change in sign in the direction of axial current flow.) Moreover, an almost (axially) current-free ( $J_z \simeq 0$ ) sheath lies between them, as can be seen in panel (2-2) of Fig. 11 ( $0.4 \lesssim |x| \lesssim 1.0$ ). The net axial current  $I_z$  must be zero to avoid the accumulation of electrical charge at the end point:

$$I_z = \int_0^{r_{\text{max}}} 2\pi (J_z^{\text{jc}} + J_z^{\text{rc}}) r dr = 0. \quad (13)$$

$r_{\text{max}}$  is located at the radius where  $B_\phi(r_{\text{max}}) = 0$ . This is similar to the transverse analytical structure used by Lind et al. (1989) as inflow conditions for their axisymmetric, toroidal field-only simulations. At intermediate times, therefore, our three-dimensional numerical simulations have the same dynamical structure as a current-carrying equilibrium jet in force balance.

A remarkable feature of the  $J_z^{\text{jc}}$  distribution is the high axial current density in the region  $5 \lesssim z \lesssim 10$  in models A – 1 and A – 2 (*Top* and *2nd* panels in Fig. 10), and low axial current density there in models B – 1 and B – 2 (*3rd* and *Bottom* panels in Fig. 10) [see also (2-2) of Fig. 11]. This is directly related to how the toroidal component of the field  $B_\phi$  increases across the first (F–F) shock/compressive and third (R–S) shock waves [or decreases across the second (F–S) shock wave]. A strong accumulation of  $B_\phi$  produces a large hoop-stress ( $-B_\phi^2/r$ ), pinching the jet towards the central axis. As a result, the gradient of the  $B_\phi$  in the transverse direction becomes larger, and  $J_z^{\text{jc}}$  along the central axis is therefore enhanced.

As discussed above, we identify an almost (axially) current-free region between the forward jet current  $\mathbf{J}^{\text{jc}}$  and the return current  $\mathbf{J}^{\text{rc}}$  densities, where  $J_z$  is close to 0 [see Fig. 10 and (2-2) of Fig. 11]. In this region the transverse component of the field  $B_y$  and velocity  $V_y$  have a maximum value and the magnetic lines of force are highly twisted (with the ratio  $B_y/B_z$  much larger than that in the central jet). We will refer to this region as the “external magnetized wind”. (The total outflow consists of both the jet *and* the wind. Here we distinguish the wind from the jet by the fact that it is not current-carrying.) In a later section we will discuss the wind’s effects on the stabilization of the jet against disruption by KH instabilities.

#### 4.2.4. Final evolutionary stages: destabilization of PFD jets

In the late stages of jet evolution (*3rd* and *Bottom* panels of each of Figs. 3–6), the jets are deformed into wiggled structures in both the density and velocity fields. For the shallow-

atmosphere, highly PFD model A – 1, the jet is distorted both beyond the second shock wave and behind the third shock wave. In addition, as the jet instabilities become fully developed, the high temperature region containing the pair of two slow-mode shock waves and the contact discontinuity between them, is fully disrupted also.

On the other hand, for models A – 2 (the shallow-atmosphere, mildly PFD case) and B – 1 (the steep-atmosphere, highly PFD case) the jets are distorted behind the second shock wave only. The high temperature region between the two slow-mode shock waves appears unaffected.

The instability appears to have the slowest growth rate in the steep-atmosphere, mildly PFD case (model B – 2), with only a slight distortion appearing behind the R–S shock wave.

Figure 12 shows snapshots of  $J_z$  in the "final stages" of all the models. Here we also see that the jet current density  $J_z^{\text{jc}}$  is distorted into the wiggled structure seen in the density and velocity fields of models A – 1, A – 2, and B – 1. In Fig. 13 we also show (in the final stages in all models and in the  $x - z$  plane close to the jet axis) the distributions of the Alfvén and sound speeds, as well as each component of the jet velocity. We identify the following features in each of the models:

- The axial speed of the jet  $V_z$  in model A – 1 is still sub-Alfvénic except at the jet head itself (the head is a F–F shock wave, and therefore, super-Alfvénic and super-fast magnetosonic); that is, the highly PFD jet remains Poynting flux dominated in this shallow atmosphere.
- $V_z$  in model A – 2 is super-Alfvénic beyond  $z > 2$  (the jet head is also a F–F shock wave); that is, the mildly PFD jet has switched to a mildly kinetic energy flux dominated (KFD) jet.
- $V_z$  in model B – 1 is trans-Alfvénic beyond  $z > 10$ , where the jet is distorted; that is, the highly PFD jet in this steep atmosphere has switched to an equipartition state between the kinetic and Poynting fluxes.
- $V_z$  in model B – 2 is super-Alfvénic beyond  $z > 2$ ; that is, the mildly PFD jet in the steep atmosphere has switched to a KFD jet.

We conclude, therefore, that jets propagating in the trans-Alfvénic region, before they become kinetic energy flux dominated ( $V_A \sim V_{\text{FM}} \lesssim V_j$ ), can be deformed into wiggled structures. We consider the physical mechanism for these destabilization in the following sections.

### 4.3. Nonlinear Growth of CD Instabilities

#### 4.3.1. Computation of the power spectrum

To better understand the nonlinear behavior of CD instabilities in our jet simulations, we begin by defining the forward jet current density  $\mathbf{J}^{\text{jc}}$  to be equal to the total current density  $\mathbf{J}$  in those places where  $J_z$  has a negative sign and zero otherwise:

$$\mathbf{J}^{\text{jc}} \equiv \begin{cases} \mathbf{J} & (J_z < 0) \\ 0 & (J_z \geq 0) \end{cases}. \quad (14)$$

We distinguish  $\mathbf{J}^{\text{jc}}$  from the jet return current density

$$\mathbf{J}^{\text{rc}} \equiv \begin{cases} \mathbf{J} & (J_z > 0) \\ 0 & (J_z \leq 0) \end{cases}, \quad (15)$$

which differs in sign from  $\mathbf{J}^{\text{jc}}$ . Note that  $\mathbf{J}^{\text{jc}}$  (and  $\mathbf{J}^{\text{rc}}$ ) is a vector and can have additional radial and azimuthal components  $J_r^{\text{jc}}$  and  $J_\phi^{\text{jc}}$  with *any* sign. (These components are computed by transforming to a cylindrical coordinate system from the simulation Cartesian coordinates.)

We now proceed to analyze the modal structure of  $\mathbf{J}^{\text{jc}}$  by forming the volume-averaged Fourier transform of its magnitude

$$\tilde{\mathbf{J}}^{\text{jc}}(m, k) = \frac{1}{V_{\text{cl}}} \iiint_{V_{\text{cl}}} |\mathbf{J}^{\text{jc}}| e^{i(m\phi + kz)} r dr d\phi dz, \quad (16)$$

where  $|\mathbf{J}^{\text{jc}}| \equiv [(J_r^{\text{jc}})^2 + (J_\phi^{\text{jc}})^2 + (J_z^{\text{jc}})^2]^{1/2}$  and  $V_{\text{cl}}$  is the annular volume that encloses  $\mathbf{J}^{\text{jc}}$

$$V_{\text{cl}} = \int_{r_a}^{r_b} \int_0^{2\pi} \int_{z_a}^{z_b} r dr d\phi dz. \quad (17)$$

We use the values  $r_a = 0.075$ ,  $r_b = 2.25$ ,  $z_a = 0.0$ , and  $z_b = 18.0$ .

$\tilde{\mathbf{J}}^{\text{jc}}(m, k)$  is now a function of the azimuthal mode  $m$  and axial wave number  $k = 2\pi/\lambda$  (corresponding to a characteristic wave length  $\lambda$ ). Like  $\mathbf{J}^{\text{jc}}$ ,  $\tilde{\mathbf{J}}^{\text{jc}}$  is a function of time.

Finally, we identify the power spectrum as the squared amplitude of  $\tilde{\mathbf{J}}^{\text{jc}}$

$$|\tilde{\mathbf{J}}^{\text{jc}}(m, k)|^2 = \left\{ \text{Re}[\tilde{\mathbf{J}}^{\text{jc}}(m, k)] \right\}^2 + \left\{ \text{Im}[\tilde{\mathbf{J}}^{\text{jc}}(m, k)] \right\}^2, \quad (18)$$

$$\begin{aligned} & \text{Re}[\tilde{\mathbf{J}}^{\text{jc}}(m, k)] \\ &= \frac{1}{V_{\text{cl}}} \iiint_{V_{\text{cl}}} |\mathbf{J}^{\text{jc}}| \cos(m\phi + kz) r dr d\phi dz, \end{aligned} \quad (19)$$

$$\begin{aligned} & \text{Im}[\tilde{\mathbf{J}}^{\text{jc}}(m, k)] \\ &= \frac{1}{V_{\text{cl}}} \iiint_{V_{\text{cl}}} |\mathbf{J}^{\text{jc}}| \sin(m\phi + kz) r dr d\phi dz. \end{aligned} \quad (20)$$

For each model we now will examine the time-dependent behavior of the power spectrum and investigate the nonlinear growth of each mode.

#### 4.3.2. Growth of azimuthal modes

We first will consider only azimuthal modes ( $m$ ) — *i.e.*, the power spectrum  $|\tilde{\mathbf{J}}^c(m)|$  for infinitesimal wave numbers ( $k \rightarrow 0$ ). Several modes ( $m = 1 - 4$ ) are plotted as functions of time in Fig. 14. Note that, while we have not imposed any explicit perturbations to our jets, they are subject to the implicit perturbations created by the 3-D Cartesian grid. As a result of our resolving an initially, rotating cylindrically symmetric object on a Cartesian coordinate, the  $m = 4$  mode appears before the physical growth of the other asymmetric modes. We find, however, that the power in the  $m = 4$  mode remains constant or decreases with time on all models. We therefore identify the level of power in the  $m = 4$  mode as our (conservative) noise level and identify all power greater than that (and in any other mode) as spectral power generated by the physical evolution of the jet.

In all models the kink ( $m = 1$ ) mode grows faster than the other higher order modes ( $m = 2, 3$ ). In Fig. 14 the time at which the kink mode appears above the “noise” level in each of the models is as follows:  $t \sim 18$  (A – 1),  $t \sim 23$  (A – 2),  $t \sim 23$  (B – 1), and  $t \sim 17$  (B – 2). In addition, in A – 1 both the  $m = 1$  and  $m = 2$  modes appear around  $t \sim 30$ , and the  $m = 3$  mode saturates at or below the noise level. In A – 2, the  $m = 2$  and 3 modes track one another and saturate at our chosen noise level. In B – 1 and B – 2, the  $m = 2$  and 3 modes also track one another and saturate at a level *lower* than that of the  $m = 4$  mode.

The  $m = 1$  mode for each model exhibits approximately exponential growth on a dynamical time scale. A linear fit using a least-squares method has been performed on the time-sequenced data to extract a linear growth rate

$$\text{Im}(\omega) \sim \frac{d \ln |\tilde{\mathbf{J}}^c(m)|^2}{dt}. \quad (21)$$

The estimated growth rates are given in Table 3 and shown on Fig. 14. The growth rate appears to be strongest for A – 2 [ $\text{Im}(\omega) \sim 0.54$ ], and weakest for A – 1 [ $\text{Im}(\omega) \sim 0.31$ ]. As seen in Fig. 14, the instability appears to have saturated in the final stages for both A – 2 and B – 2 (the mildly PFD models), but still appears to be growing for both of the highly PFD models A – 1 and B – 1.

How do these growth rates compare with the Alfvén crossing time scale, which is typically the time scale on which pure CD modes can develop (Begelman 1998; Appl, Lery, & Baty 2000; Lery & Frank 2000)? The spatial length scale of the CD instability in our results (in the radial direction) is of the order of a jet width,  $L \sim 1.0$  (see Fig. 12). The local  $V_A$  in the distorted jet portion is of order 0.3 – 0.8, as seen in Figs. 7 and 13. So, the inverse of the Alfvén crossing time

$\tau_A^{-1}$  in the distorted jets is approximately given by

$$\tau_A^{-1} = \frac{V_A}{L} \sim 0.3 - 0.8. \quad (22)$$

This is, in general, consistent with the time scales of the growing  $m = 1$  modes derived from Fig. 14,

$$\text{Im}(\omega) \approx O(\tau_A^{-1}). \quad (23)$$

#### 4.3.3. Development of the $m = 1$ helical kink

Figure 15 shows a space-time  $(z, t)$  plot of the ratio of the transverse and axial magnetic field components  $-B_y/B_z$  for model A – 1, illustrating the dynamical evolution of the helically kinked magnetic field. Propagation of the jet head, corresponding to a F–F compressive wave front, can be seen. The wave gradually decelerates due to the decreasing ambient  $V_A$  until  $t \sim 15$ ; after that it propagates with an almost constant phase velocity. The amplitude of the F–F compressive wave grows significantly with time and could steepen into a F–F shock wave (bow shock) with subsequent evolution. After  $t \sim 20$ , the kinked part of the field appears behind the R–S first, and later, it appears in the upstream region. Finally, the flow downstream (between the F–F and the F–S) is also kinked. We can see that *the kinks in these three regions grow independently, and the peaks of the kinked magnetic field simply co-move with the jet*. These characteristics indicate that *the CD kink mode does not propagate in the jet rest frame* (Appl 1996). This behavior is quite different from that of the KH instability. In the latter case, the disturbance propagates *backwards* in the jet rest frame, because the phase velocity of the KH modes is smaller than the jet velocity, which must be super-Alfvénic to stimulate the KH unstable modes.

Figure 16 shows snapshots of the radial specific power generated by the Lorentz force on two-dimensional  $x - z$  slices at  $y = 0$ . This is defined as the work done per unit mass in the  $r$ -direction in a cylindrical coordinate system  $(r, \phi, z)$ :

$$(\mathbf{J} \times \mathbf{B})_r V_r / \rho, \quad (24)$$

where

$$(\mathbf{J} \times \mathbf{B})_r = -J_z B_\phi + J_\phi B_z.$$

If we consider only radial variations in the Lorentz force, then

$$-J_z B_\phi = -\frac{B_\phi}{r} \frac{\partial}{\partial r} (r B_\phi),$$

and

$$J_\phi B_z = -B_z \frac{\partial B_z}{\partial r}.$$

There is a strong correlation between this power distribution and the wiggled structures seen in A – 1, A – 2, and B – 1. This is consistent with our early finding that the disruption occurs only locally where the MHD jet is CD unstable. That is, *distortions do not propagate*. These snapshots also lead us to conclude, as we did in Fig. 14, that the CD instability is still growing for the highly PFD jets A – 1 and B – 1, but is almost saturated for the mildly PFD flows A – 2 and B – 2. This means that the magnetic field in the flow should be in “radial” force-free equilibrium ( $\mathbf{J} \times \mathbf{B} \simeq 0$ ) in the saturated models.

We conclude that CD instabilities grow during the simulation evolution even without the addition of small perturbations to the system. This is because we have performed computations with high enough resolution to amplify asymmetric modes from the numerical background noise. We close this section by noting that the instabilities reported here do not arise if we choose a grid spacing that is two or more times larger than the current one. The effects of numerical diffusion appear to damp out the growth of the CD instability in this case.

## 4.4. Stabilization of the CD Instability with Rapid Rotation

### 4.4.1. The Classical Kruskal–Shafranov Criterion

According to the well-known Kruskal–Shafranov (K–S) criterion (Shafranov 1957; Kruskal et al. 1958), which is based on a skin-current model, a magnetized flux tube (along the  $z$  axis) is stable to the CD kink ( $m = 1$ ) mode as long as the magnetic twist angle  $\Phi(r)$  is below some critical value  $\Phi_{\text{crit}}$ ,

$$\Phi(r) \equiv \frac{LB_\phi}{rB_z} < \Phi_{\text{crit}}, \quad (25)$$

where,  $L$  is the length of the current-carrying magnetic flux system,  $r$  is the radius of the flux tube, and  $B_z$  and  $B_\phi$  are the axial and azimuthal field components in cylindrical coordinates, respectively. Many theoretical and numerical investigations have been performed on the current-driven stability problem of solar coronal loops, and the K–S criterion plays an important role in those studies.

In the original K–S criterion,  $\Phi_{\text{crit}}$  is set equal to  $2\pi$ . The effects of line-tying, *i.e.*, anchoring the axial boundary conditions on the magnetic field in a high-density photosphere, however, raise the stability threshold. The modified critical values for a force-free configuration are between  $2\pi$  and  $10\pi$  (Hood & Priest 1979; Einaudi & Van Hoven 1983).

For a jet configuration, which has  $L \gg r$ , we replace  $L$  by a spectrum of axial wavelengths  $\lambda$ , and we define the critical wavelength to be the one that is marginally stable

$$\begin{aligned}\lambda_{\text{crit}} &\equiv \frac{\Phi_{\text{crit}} r B_z}{B_\phi} \\ &= \frac{2\pi r B_z}{B_\phi}.\end{aligned}\tag{26}$$

The K–S stability criterion (eq. 25) then becomes

$$\lambda < \lambda_{\text{crit}},\tag{27}$$

so that wavelengths greater than  $\lambda_{\text{crit}}$  are unstable to the CD instability. From a computational point of view,  $\lambda$  must lie in the range

$$\Delta \leq \lambda \leq L(t),\tag{28}$$

where  $\Delta$  is the minimum grid width and  $L(t)$  is time-dependent jet length, with maximum value  $L_{\text{max}}(t)$  dependent on the computational domain. In practice, however, shock waves and other MHD phenomena provide effective domain boundaries, so that the maximum value of  $\lambda$  could be only a fraction of the entire jet length.

#### 4.4.2. Force Balance in Rotating Jet Systems

Because real astrophysical jet systems may be rotating, the K–S criterion may not be an adequate stability condition for the CD kink mode. Rotation will modify the radial force balance inside jet. Although rotation is often neglected in theoretical models of jet equilibrium (Begelman 1998; Appl, Lery, & Baty 2000), it could play an important role in the stability analysis. Let us consider the time-independent, force-balance equation (2) in the radial direction. In an inertial frame co-moving with the jet we have

$$-\nabla P + \mathbf{J} \times \mathbf{B} + \hat{r}\rho\Omega^2 r = 0,\tag{29}$$

where  $\Omega$  is the equilibrium angular velocity and  $\hat{r}$  is the unit vector in the  $r$  direction. It is clear that the axial flow velocity  $V_z$  does not affect the radial force balance, but the presence of an *azimuthal* velocity component can have a significant influence on the equilibrium, modifying the competition between the pressure gradient and the Lorentz force. Moreover, our PFD jets are strongly magnetized ( $\beta \ll 1$ ), so the pressure gradient term on the left-hand side of equation (29) can be neglected. This yields

$$-\frac{\partial}{\partial r} \left( \frac{B_\phi^2 + B_z^2}{2} \right) - \frac{B_\phi^2}{r} + \frac{\rho V_\phi^2}{r} = 0,\tag{30}$$

where  $V_\phi$  is the equilibrium azimuthal velocity. The first term on the right-hand side in equation (30) is the magnetic pressure gradient in both the azimuthal and axial components. These forces are positive or negative depending on whether  $B_z$  and  $B_\phi$  decrease or increase with  $r$ , respectively. The second term is the magnetic tension force (hoop-stress), which is always directed inward (in the  $-r$  direction). The third is the centrifugal force, which always acts in the  $+r$  direction, opposite to the hoop-stress.

One key parameter of radial equilibrium in rotating jets is the radial index  $\kappa$  of the magnetic pressure  $p_m^* = (B_\phi^2 + B_z^2)/2$  gradient

$$\kappa \equiv \frac{\partial \log p_m^*}{\partial \log r}. \quad (31)$$

Under the assumption that the magnetic field strength decreases outward near the jet surface,  $\kappa$  should be less than zero. Furthermore, for specific cases of analytically asymptotic solutions for cylindrically symmetric axial flows with power-law radial distributions of the physical quantities, a lower limit on  $\kappa$  must exist (Ostriker 1997). The magnetic field strength  $|B^*| [\equiv (B_\phi^2 + B_z^2)^{1/2}]$  must decline with  $r$  more slowly than  $r^{-1}$  to ensure force balance and cylindrical collimation. (That is, the magnetic field cannot have a gradient so steep that the corresponding magnetic pressure force will exceed the hoop-stress.) Taken together, these conditions require  $-2 \leq \kappa < 0$ .

We now introduce another key parameter, the azimuthal (toroidal) Alfvén Mach number:

$$M_{A\phi} \equiv \frac{V_\phi}{V_{A\phi}}, \quad (32)$$

where  $V_{A\phi} \equiv |B_\phi|/\sqrt{\rho}$ . In the present paper, we have excluded the situation that jets are confined solely by the external hot ambient medium. So, to prevent radial expansion of the self-collimated jets with  $\kappa < 0$ , an upper-limit on  $M_{A\phi}$  should be set:

$$M_{A\phi} \leq 1. \quad (33)$$

In the following sections, we will consider these two key parameters as diagnostics of radial force equilibrium in the rotating MHD jets.

#### 4.4.3. *Non-rotating strongly magnetized jets*

If the jet has a low plasma- $\beta$  ( $\ll 1$ ) and is non-rotating ( $M_{A\phi} = 0$ ), the magnetic field in the jet will be in force-free equilibrium

$$-\frac{\partial}{\partial r} \left( \frac{B_\phi^2 + B_z^2}{2} \right) - \frac{B_\phi^2}{r} = 0, \quad (34)$$

That is, the gradient of the magnetic pressure will be balanced by the magnetic hoop-stress. Various types of the force-free equilibrium in jets have been investigated for different radial profiles of the magnetic twist  $\Phi(r)$  (Appl, Lery, & Baty 2000; Lery, Baty, & Appl 2000). For astrophysical jets of magnetic origin, the azimuthal field is likely to be dominant, and the properties of the fastest growing CD kink ( $m = 1$ ) mode become nearly independent of the details of the pitch profile (Appl, Lery, & Baty 2000).

#### 4.4.4. Rotating strongly magnetized jets

If the jet is rotating ( $M_{A\phi} > 0$ ), an equilibrium *force-free* magnetic field will not be possible. The inertia of the rotating plasma will play an important role in jet stability as  $M_{A\phi}$  becomes large. This situation is quite different from the one that occurs in solar coronal loops.

For an azimuthally sub-Alfvénic flow ( $0 < M_{A\phi} < 1$ ) in equilibrium, equation (30) will be satisfied. The hoop-stress is the only force acting inward and this must be balanced by the outward centrifugal and magnetic pressure gradient forces ( $\kappa < 0$ ).

For an azimuthally trans-Alfvénic flow  $M_{A\phi} \sim 1$ , the gradient of the magnetic pressure becomes zero (*i.e.*,  $\kappa \sim 0$ ), and force-equilibrium between the hoop-stress and the centrifugal force holds:

$$-\frac{B_\phi^2}{r} + \frac{\rho V_\phi^2}{r} = 0. \quad (35)$$

If the radius  $r$  of the magnetized loop increases slightly, the centrifugal force will fall off faster than the hoop-stress, causing an inward-directed net magnetic tension that returns the loop to its original size. On the other hand, if  $r$  decreases slightly, the hoop-stress increase less rapidly than the centrifugal force, causing an outward-directed net centrifugal force that again returns the loop to its original size. Rapid rotation, therefore, has a potentially stabilizing effect on traditionally unstable twisted magnetic configurations.

#### 4.4.5. Numerical results for non-rotating and rotating jets: growth of axial modes

We now inspect our numerical results more closely and analyze the stabilizing effects of rotation against the CD kink mode. We will continue to use the Fourier power spectrum analysis, applying it to the  $m = 1$  mode and also extending it to growing modes in the axial ( $k$ ) direction. We also will re-examine the distribution of  $J_z$  and study a correlation between the maximum allowable magnetic twist  $\Phi(r)$  and the toroidal Alfvén Mach number  $M_{A\phi}$  for some selected parts of the jets.

Figure 17 (1) shows a space-time  $(\lambda, t)$  diagram of the power spectrum of  $|\tilde{\mathbf{J}}^c(1, \lambda)|$  for model A – 2. The shortest wavelength physically growing  $m = 1$  mode is  $\lambda_{\min} \sim 1.0$ ; perturbations with wavelength longer than this already have started growing by  $t = 15.0$ . An enlarged snapshot of  $J_z$  for A – 2 at  $t = 19.5$  (from Fig. 10) also is shown in Fig. 17 (2). Note the wiggled structure behind (upstream of) the R–S point with a destabilization length of  $\lambda \sim 2.0$ . The 3rd panel of Fig. 17 (3) shows the transverse profiles from panel (2) of  $\Phi(r)$  (for  $\lambda = 2.0$ ) and of  $M_{A\phi}$  at two different axial positions in the jet ( $z=6.1$  and  $8.3$ ).

The value of  $\Phi(r)$  at the point  $z = 6.1$  increases gradually towards the inner jet. It exceeds the K-S critical value  $\Phi_{\text{crit}} = 2\pi$  for radial position  $|x| \lesssim 0.4$  and has a maximum ( $\sim 10$ ) near the jet axis. At  $z = 8.3$ , on the other hand,  $\Phi(r)$  shows a sharp rise inward and has already exceeded  $\Phi_{\text{crit}}$  by  $|x| \sim 1.0$ . Between  $0.4 \lesssim |x| \lesssim 1.0$ , the magnetic twist is very large ( $\gtrsim 20$ ), followed by a sharp fall to around  $\sim 10$ .

The values of  $M_{A\phi}$  at both axial points decrease gradually towards the inner jet, approaching close to 0 within  $|x| \lesssim 0.4$ . Because there is little rotation in the region  $|x| \lesssim 0.4$ , the classical K–S criterion (25) can be used to analyze the stability of this shallow-atmosphere, mildly PFD case jet. Noting that the twist  $\Phi(r)$  exceeds the K–S limit at  $z = 8.3$  throughout most of the body of the jet, we conclude that the jet at that point is already unstable to the CD kink mode. On the other hand, because at  $z = 6.1$  the K–S criterion is moderately violated in the region  $|x| \lesssim 0.4$ , we conclude that the flow in this model is beginning to go unstable to the CD kink mode at that point.

Figure 18 performs a similar analysis for another model from Fig. 10 — the shallow-atmosphere, highly PFD case A – 1. In this case, the shortest wavelength physically growing  $m = 1$  mode changes with time, gradually shifting from  $\lambda_{\min} \sim 2.5$  to  $\sim 1.0$ . However, at the chosen model time ( $t = 21.5$ ), perturbations with  $\lambda \lesssim 2.0$  have not yet started growing. [Compare Fig. 10 and Fig. 18 (1) and (2)]. Yet, in Fig. 18 (3), the values of the magnetic twist  $\Phi(r)$  at *both* axial positions ( $z = 6.1$  and  $8.3$ ) appear to exceed the critical  $\Phi_{\text{crit}}$  for  $|x| \lesssim 0.4$  and have a maximum ( $\sim 10$ ) near the center.

The reason for this seeming violation of the K–S stability criterion, and yet apparent jet stability, can be seen in the  $M_{A\phi}$  plot in Fig. 18 (3). The value of the azimuthal Mach number at both axial points is *large for all radii in the jet*, never dipping below  $M_{A\phi} \sim 0.5$ . The large rotational velocity of the jet in this case provides a stabilizing influence over the classical K–S criterion throughout this jet region.

Our nonlinear numerical results are consistent with the linear theory. A linear stability analysis of the CD  $m = 1$  mode was performed for a non-rotating cold (strongly magnetized) jet (in force-free equilibrium) by Appl (1996) and Appl, Lery, & Baty (2000). They showed that the most unstable wavenumber  $k_{\max}$ , as well as the maximum growth rate  $\text{Im}(\omega)_{\max}$ , are only slightly

affected by the jet (axial) velocity  $V_j$  and the radial profile of the magnetic pitch  $rB_z/B_\phi$ . (Note that the decrease of  $\text{Im}(\omega)$  with increasing  $M_A = V_j/V_A$  in their papers is associated with a decrease in  $V_A$ , not an increase in  $V_j$ .) In our results, unstable axial modes are excited over a large wavelength range. However, the wavelength  $\lambda_{\text{max}}$  corresponding to  $k_{\text{max}}$  seems to occur in the range  $2 < \lambda_{\text{max}} < 3$  for both the super-Alfvénic ( $A - 2$ ) and sub-Alfvénic ( $A - 1$ ) cases [see Figs. 17 (1) and 18 (1)]. Therefore, we do not see a strong correlation between  $k_{\text{max}}$  and  $M_A$  in our results, and this is qualitatively consistent with the linear analysis.

These results lead us to conclude that the classical K–S criterion holds in approximately non-rotating jets (even the nonlinear regime), but that rotation in a jet creates a stabilizing effect against the CD kink mode. *Rotating jets can remain stable even when the magnetic twist exceeds the classical K–S criterion.*

#### 4.5. Sudden Destabilization of a Jet by Angular Momentum Loss

Having shown that the  $V_\phi$  velocity component plays an important role in stabilizing the jet, we now investigate how the jet behaves if that rotation is suddenly removed. When  $\beta \ll 1$ , if  $V_\phi$  were to decrease gradually as the jet propagates, *e.g.*,  $V_\phi \propto z^{-1}$ , then the magnetic field in the jet would shift quasi-statically toward a force-free ( $\mathbf{J} \times \mathbf{B} \simeq 0$ ) configuration. However, if part of the jet suddenly loses its toroidal velocity through some dynamical means, then that part will subject to a non force-free magnetic field ( $\mathbf{J} \times \mathbf{B} \neq 0$ ). Here we investigate the sudden loss of rotation as a possible trigger process for the CD instability.

##### 4.5.1. The principal driving force of the CD kink

First, we shall determine the principal driving force of the CD kink ( $m = 1$ ) mode. Transverse profiles of the physical quantities in the intermediate stage at axial position  $z = 8.3$  are plotted in Fig. 19. Panel (1) shows the specific centrifugal ( $V_\phi^2/r$ ) and hoop-stress ( $-B_\phi^2/r/\rho$ ) forces for all four models. Panel (2) shows the distribution of magnetic pressure contributed by both the azimuthal and axial components  $p_m^* = (B_\phi^2 + B_z^2)/2$ .

In both models B – 1 and B – 2, the centrifugal force is balanced by the hoop-stress, so the flows are *azimuthally* trans-Alfvénic ( $M_{A\phi} \sim 1$ ). In addition, the magnetic pressure in these two models has quite a small gradient and so contributes little to the radial force balance. The flow is apparently CD stable at this axial position ( $z = 8.3$ ), so we conclude that the azimuthal rotation has stabilized the flow.

In model A – 1, the centrifugal force is smaller than the hoop-stress, so the flow is azimuthally sub-Alfvénic ( $M_{A\phi} < 1$ ) and has a significant magnetic pressure gradient working with the centrifugal force to balance the hoop-stress. It is noteworthy, however, that the position of the magnetic pressure peak lies at the center of the jet  $(x, y)=(0, 0)$ : the force balance on either side of the jet is therefore symmetric. This situation is also apparently CD stable.

In model A – 2, however, the relative contribution of the centrifugal force is essentially zero ( $M_{A\phi} \simeq 0$ ). The only forces trying to remain in balance are the magnetic hoop-stress and the radial magnetic pressure gradient. Figure 19, however, shows that these forces are not able to maintain a symmetric distribution as they try to balance each other. The hoop-stress at this axial position is asymmetric, and the (otherwise symmetric) magnetic pressure profile peak has been pushed to a position offset from the axis. *The 3-D response of a force-free magnetic configuration to asymmetric hoop-stress, then, is not to create an asymmetric magnetic pressure profile but rather to push that symmetric profile off to one side.* This asymmetry indicates that the CD modes have already begun to grow to a measurable level, and that this part of the jet is being accelerated in a negative radial direction ( $-x$ ).

We conclude that the CD instability is driven by asymmetric hoop-stress, created in a region of large magnetic twist, which cannot be balanced stably by a corresponding asymmetric magnetic pressure gradient.

#### 4.5.2. Origin of the very large magnetic twist

We now examine the origin of this high magnetic twist in the jet. The twist is characterized by a relatively large  $|B_\phi|$  and a small  $B_z$ .

Figure 20 shows the intermediate-stage radial profiles (parallel to the  $r$ -axis along  $\phi = 0$ ) of each component of the magnetic field ( $|B_\phi|$  and  $B_z$ ) and the magnetic pressure  $p_m^*$ , as well as the initial distribution of the axial field component  $B_z^{\text{init}}$  (same for all models). As we saw in Fig. 19 (2), the distributions of the magnetic pressure for B – 1 and B – 2 are flat. This creates separate  $|B_\phi|$  and  $B_z$  distributions that are low and high at different radii.

For models A – 1 and A – 2 we see that, in the region  $0.3 \lesssim r \lesssim 1.0$ , the magnetic pressure follows  $\kappa \sim -1$  and  $\kappa \sim -2$  distributions, respectively. Of particular interest in these plots is the behavior of  $B_z$  at these intermediate radii. Compared with the initial distribution, the axial field becomes stronger at small radii ( $r \lesssim 0.3$ ) and remains about the same strength at large radii ( $r \lesssim 1.5$ ). However, in the region  $0.3 \lesssim r \lesssim 1.5$  it dips *substantially*, particularly for model A – 2 in Fig. 20.

We conclude that the very large magnetic twist (which leads to asymmetric hoop stress and a CD instability) is caused not so much by a large increase in  $B_\phi$  as by a large *decrease* in  $B_z$  at intermediate radii [see, especially, Fig. 17(3)].

#### 4.5.3. *Origin of the weak axial field causing the large twist: triggering of the CD kink instability by the reverse slow-mode shock*

Finally, we shall identify the physical mechanism that causes  $B_z$  to decrease and create the strong magnetic twist. In particular, this will occur when rotation is suddenly removed from the jet flow, triggering the pinch. We find that this occurs at a number of places in the jet flow, but is particularly strong right behind the R–S shock wave.

Figure 21 shows in the intermediate evolutionary stage offset axial profiles (parallel to the  $z$ -axis, at  $(r, \phi)=(0.5, 0)$ ) of each component of the magnetic field and velocity. All models begin with the same power-law distribution of  $B_z$  with  $z$  [see panel (1)]. However, only model A – 2, and to a lesser extent A – 1, develop a large region of substantially low  $B_z$ , especially in the region  $8.0 \lesssim z \lesssim 10$ .

As pointed out in Sec. 4.2.2, there is a sudden rise in  $|B_\phi|$ ,  $V_z$ , and  $V_\phi$  around  $z = 10.0$  for all models [see Fig. 21 (2), (3), and (4)], which corresponds to the passage of the F–F compressive/shock wave front. The models split into two classes [see panels (2) and (4)]: those with a large enhancement in  $|B_\phi|$  and a small enhancement of  $V_\phi$  (A – 1 and A – 2) and those with a small enhancement in  $|B_\phi|$  and a large increase in  $V_\phi$  (B – 1 and B – 2).

A large enhancement in  $|B_\phi|$ , with a small enhancement in  $V_\phi$ , indicates that a considerable amount of energy has been converted from the toroidal (rotational) kinetic energy in the TAW to toroidal magnetic energy behind the F–F shock wave front.

The sudden drop of both  $|B_\phi|$  and  $V_\phi$  at  $z = 9.2$  in model A – 2 (dashed lines) and at  $z = 5.5$  for B – 2 (dotted lines) occurs with the passage of the F–S shock wave front. We also can identify the R–S shock wave front near axial position  $z = 8.5$  for model A – 2. At this point  $|B_\phi|$  is enhanced once again (panel (2)), but  $V_\phi$  has a sharp dip before rising to its injected value for  $z < 8.0$ . The contact discontinuity lies in between the two slow-mode shock waves — at  $z \sim 8.7$ .

The behavior of these quantities at the R–S shock wave is especially interesting. While  $|B_\phi|$  simply increases, the dip in  $V_\phi$  has important consequences. In this transition, part of the jet near  $z = 8.3$  loses toroidal velocity (angular momentum) but still gains enhanced toroidal magnetic field. The centrifugal support against the hoop-stress, therefore, is lost, causing a sudden squeezing of of the poloidal magnetic flux  $|\mathbf{B}_p| \equiv (B_r^2 + B_z^2)^{1/2}$  towards the central ( $z$ ) axis. As a result, a

concentration of  $B_z$  flux occurs at the jet center ( $r \lesssim 0.3$ ), *at the expense of  $B_z$  flux at intermediate radii* ( $0.3 \lesssim r \lesssim 1.5$ ) (see also A – 2 in Fig. 20).

To summarize, we believe that the CD kink mode is triggered as follows. The process begins when rotating, magnetized jet material experiences a sudden loss of kinetic angular momentum to the magnetic field. This destroys the (stable) balance between centrifugal force and hoop-stress, producing a strong pinch of  $B_z$  flux toward the  $z$  axis, depleting  $B_z$  flux in the intermediate radial region of the jet, and further enhancing the magnetic twist. With no rotation to stabilize this large twist, the K–S criterion is suddenly strongly violated and the jet becomes unstable to the CD kink mode. Any slight radial asymmetry in the hoop-stress produces a helical kink in the current, with no stabilizing restoring force. This process can occur at various places in the jet flow, but appears strongest right behind the R–S shock wave, where there can be a pronounced dip in the rotational velocity. We believe that this is one of the most promising physical processes for producing a CD kink instability in rotating jets.

#### 4.6. Suppression of MHD KH Instabilities due to the External Magnetized Winds

We now show how the helically magnetized winds that surround the core of the jet can suppress MHD KH instabilities.

The modified stability criterion for MHD KH instabilities is as follows (Hardee & Rosen 2002):

$$\Delta V^2 - V_{As}^2 < 0, \quad (36)$$

where  $\Delta V \equiv V_j - V_e$  is the velocity shear between the jet and the external medium, and  $V_{As} \equiv [(\rho_j + \rho_e)(B_j^2 + B_e^2)/(\rho_j \rho_e)]^{1/2}$  is the surface Alfvén speed. Inequality (36) shows that a magnetic field and an outgoing wind in the external medium act to stabilize the flow against MHD KH surface modes. Figure 22 shows, for all four of our simulations, the transverse profiles in the  $x$  direction of the difference between  $\Delta V^2$  and  $V_{As}^2$ , as well as the total Alfvén Mach Number  $M_A$  ( $\equiv |\mathbf{V}|/V_A$ ). Two different evolutionary stages are compared: the intermediate stage at axial position  $z = 8.0$  and the final stage at  $z = 14.0$ .

In the intermediate stage, the MHD flow becomes trans- to super-Alfvénic for model A – 2, but remains sub-Alfvénic for all other models, as shown in Fig. 22 (1-2). Moreover, for model A – 2  $M_A$  varies smoothly at a radius ( $r \sim |x| \sim 0.4$ ), roughly the boundary between the current-carrying jet and the outer magnetized wind (see also Fig. 11). As is seen in Fig. 22 (1-1), inequality (36) is satisfied for all models, independent of the absolute value of  $M_A$ . (Note that the distribution for A – 2 is already slightly asymmetric, even though the flow is stable to MHD KH instabilities.

This indicates that the helical kink that develops must be caused by not the MHD KH instability but another possible mechanism — the MHD CD instability in this case.)

In the final stages, the flow of jet still remains sub-Alfvénic for model A – 1, but trans- to super-Alfvénic for all other models, as shown Fig. 22 (2-2). By this time all of these current-carrying jet systems, except model B – 2, have been distorted by the CD instability. As a result, the distributions of  $M_A$  for the three distorted models are decidedly asymmetric. Note that, whether the instability has grown (A – 1, A – 2, and B – 1) or not (B – 2), inequality (36) still holds everywhere for these models.

We conclude that the MHD KH surface modes are effectively suppressed, because the external magnetized winds reduce the velocity shear in the transverse direction. Our MHD jets, therefore, are distorted not by KH instabilities but pure CD instabilities, even when the flow itself becomes super-Alfvénic.

#### 4.7. Entrainment of Ambient Material in PFD Jets

In Fig. 23 we plot the axial profiles of the density and the ratio of Alfvén and sound speeds in the final stage (similar to Fig. 1). Note that the distributions of mass entrainment and  $V_A/C_s (\approx \beta^{-1/2})$  depend not on the initial conditions (initial gradients in the ambient medium), but on the nature of the flow itself (on whether it is strongly Poynting flux dominated or not). As the jets propagate through the ambient medium, they adjust themselves to the decreasing external pressure. If the ambient medium has no significant field strength ( $\beta \gg 1$ ), the jets expand, the density ratio  $\rho_j/\rho_e$  becomes smaller, and the jets are rarefied. In this case, the gradient of the external medium may play a crucial role in the entrainment of matter.

However, in the opposite case ( $\beta \ll 1$ ), the jets have considerable field strength and are prevented from expanding by the self-confining hoop-stress. This means the external density gradient might not have as much influence on mass entrainment.

The mass entrained in the mildly PFD flows is much greater than in the highly PFD flows. In particular,  $\rho$  decreases slower than  $\sim z^{-1}$  for both models A – 2 and B – 2, but roughly as  $\sim z^{-2}$  for models A – 1 and B – 1 as seen in the *Upper* panel of Fig. 23. This is partly due to the difference in injected mass flux into the computational domain. (Low mass flux implies high Poynting flux.) However, some of the effect also appears to be related to the initial ambient density gradient, with a steep atmosphere causing a higher mass entrainment in jets than the slowly decreasing case. The highest entrainment occurs for model B – 2, where the flow is both mildly PFD *and* the atmosphere has an initially steep density gradient. An enhanced mass distribution also can be seen in model B – 1, even though it is highly Poynting flux dominated. On the other hand, for model A – 1, which

neither is mildly PFD nor has an initially steep density gradient, essentially no enhancement (in fact, a slight decrease) can be seen. Denser jets in general are predicted to remain stable against MHD KH instabilities beyond the Alfvén surface and have been found to be more robust than their less dense counterparts (Hardee, Clarke, & Rosen 1997).

The  $V_A/C_s$  distributions also depend strongly on the nature of the flow as seen in the *Lower* panel of Fig. 23. Compared with their initial distributions of  $V_A/C_s$ , all models except A – 2 become significantly flattened in the  $z$  direction. Only this shallow-atmosphere, mildly PFD model, develops an even steeper distribution  $\beta^{-1/2}$ .

Even with this mass entrainment, however, our jets still keep their highly magnetized state  $V_A/C_s \gtrsim 3$  ( $\beta \lesssim 0.1$ ) during their dynamical evolution, except in the region right behind the F–F compressive/shock wave front where compression is high.

#### 4.8. Saturation and Advection of Kinked Jet Structures

As we have seen in Fig. 15 and 16, the patterns created by the CD instability can be advected by the propagating jet even after saturation of that instability has occurred. This means that *the CD instability does not destroy the interior of the jet*. Rather, it only distorts the interior into a semi-permanent wiggled structure. In the final stage of the dynamical evolution, the jets still remain strongly magnetically dominated ( $\beta \lesssim 0.1$ ), and the flow never attains a state of MHD turbulence (which requires  $\beta \gg 1$ ). If the magnetic diffusion time scale (*i.e.*, dissipation time scale of the current) is much longer than the jet propagation time scale for trans-Alfvénic flow (the Alfvén transit time scale) (Koide, Nishikawa, & Mutel 1996), these patterns will persist for some time as the flow advances. And the plasma flow itself will appear to travel in a true helical pattern as it follows the magnetic backbone of the helix (see the velocity vectors in Figs. 12 and 16).

## 5. CONCLUSIONS AND APPLICATION

### 5.1. Summary and Conclusions

By performing 3-D non-relativistic MHD simulations we have investigated in detail the nonlinear dynamics of PFD jets and the development of asymmetric instabilities. The PFD jets, powered by TAWs, propagate into extended stratified atmospheres. The presence of various compressive MHD waves in jets, which can steepen into MHD shock waves, plays an important role in the nonlinear evolution of the system. Effects such as shock waves or re-distribution of the axial current profile in the post-shocked region strongly affect the excitation of the CD instabilities.

The growth of the CD  $m = 1$  mode causes a kinked, 3-D spatial helical structure, which may be responsible for the wiggled structures seen in images of some observed jets.

We have performed four simulations with different combinations of the following initial parameters: highly ( $F_{E \times B}/F_{\text{tot}} \sim 0.9$ ) or mildly ( $F_{E \times B}/F_{\text{tot}} \sim 0.6$ ) PFD jets with decreasing or constant  $V_A$  external ambient medium along the central axis ( $z$ ). From these simulations we conclude the following:

1. Due to a centrifugal effect, rotating jets can be stabilized against the CD kink mode beyond the point predicted by the classical K-S criterion. Radial force balance in strongly magnetized ( $C_s^2 \ll V_A^2$ ) rotating jets, therefore, can involve a centrifugal force component; it need not involve only a pure electromagnetic force-free field.
2. Non-rotating jets will be subject to the CD kink mode when the classical K-S criterion is violated. The kink ( $m = 1$ ) mode grows faster than the higher order modes ( $m > 1$ ).
3. The driving force of the CD kink mode is an asymmetrically distribution of hoop-stress (the magnetic tension force). This is caused by a sudden decrease of jet rotation and a concentration the poloidal magnetic flux toward the central axis via nonlinear processes that occur at a reverse slow-mode MHD shock wave. As a result, the magnetic twist become larger than the critical value specified by the K-S criterion.
4. The linear growth rate of the CD kink mode does not depend on the flow speed. Instead, it grows on time scales of order of the local Alfvén crossing time. Kinetic-flux dominated jets that have a large Alfvén Mach number  $M_A$  ( $\sim M_{\text{FM}}$  in  $C_s^2 \ll V_A^2$ ) are not subject to the CD kink mode, because the jet propagation time is shorter than the CD instability growth time.
5. We do not see growing surface modes of the MHD KH instability even when our flows become super-Alfvénic. The naturally-occurring, external helically magnetized wind, which is (quasi-) axially current-free ( $J_z \simeq 0$ ), surrounds the well-collimated current-carrying jet. This wind reduces velocity shear between the jet and the external medium, suppressing the growth of KH surface modes. Therefore, we have been able to investigate exclusively the nonlinear behavior of pure CD instabilities.
6. Under strongly magnetized ambient conditions, the amount of mass entrained and the ratio  $V_A/C_s$  in the jet depend critically on the nature itself of the flow (*i.e.*, on the level of Poynting flux domination) and much less on the external density or gas pressure gradients. The properties of jets observed thousands of Schwarzschild radii from the galactic center, therefore, may nevertheless carry important clues about the nature of the central engine itself.

The results presented in this paper are valid in the non-relativistic regime. For relativistic motion ( $V \approx c$ ), the electric field  $\mathbf{E}$  may be comparable to the magnetic field  $\mathbf{B}$ , but it will never dominate ( $\mathbf{B}^2 - \mathbf{E}^2 > 0$  in the force-free limit). As in these non-relativistic simulations, therefore, the CD instabilities will not propagate in the rest frame of the jet (jet co-moving frame). If we choose the inertial frame to be the rest frame of the jet fluid,  $\mathbf{E}$  will vanish for a perfectly conducting fluid (the MHD condition). With  $\mathbf{E}$  (and the displacement current  $\mathbf{D}$ ) negligible, the rotation of a relativistic PFD jet (in which the energy density of the electromagnetic field is much greater than that of the particles) still will play an important role in stabilizing the flow against the growing CD instability, even in the relativistic limit. Full treatment of nonlinear CD instabilities in relativistic PFD jets will be given in a forthcoming paper.

## 5.2. The CD Instability as the Origin of Kinked Structure in AGN and Pulsar Jets

The behavior of our simulations is consistent with helical flows seen in such sources as 3C 345 (Zensus et al. 1995) and 3C 120 (Gomez et al. 2001). Helical structures appear to persist for longer than component propagation times, and the plasma components themselves appear to propagate on helical trajectories.

Of course, a three-dimensional helical shape in a real jet could be produced by precessional motion at the jet origin instead of by asymmetric CD ( $m > 0$ ) modes. In both cases the center of the actual jet flow would deviate from the jet central axis during dynamical evolution. However, precessional jets do not show true helical motion as their components move outward from the galactic center. They simply move ballistically, with the turning radius becoming larger as the jet moves further from the origin.

In the case of asymmetric KH surface modes, such a deviation of the flow from the jet axis is not even possible (see, *e.g.*, Fig. 5 in Hardee & Stone 1997). While it might be so for the asymmetric KH “body” modes, the growth range for these modes is limited (see, 2.4.1).

Therefore, if most parsec-scale helical jets in AGN are confirmed to be true helical flows, then the CD instability in a Poynting flux dominated jet may be a viable model for producing the kinked, helical structures seen in these objects. An excited wave disturbance, such as occurs in a KH mode, may not always be needed in order to explain the kinked morphological features in these jets.

High angular resolution, time-dependent X-ray observations by the *Chandra* X-ray observatory displayed year-scale variations in jet morphology in the Vela (Pavlov et al. 2003) and Crab (Mori et al. 2004) pulsar wind nebulae. These sources showed a growth of their overall kinked structure as the jet moves outward. The Crab jet is 10 times larger and varies 10 times more slowly

than the Vela jet. (Time scales and jet widths are 150-500 days and  $2.9 \times 10^{17}$  cm for the Crab, and 10-30 days and  $3.0 \times 10^{16}$  cm for Vela, respectively.) These kinked patterns seem to be co-moving with the main flow, and the time scales reported are proportional to the Alfvén crossing time (with  $V_A$  being approximately the speed of light for these ultra-relativistic plasmas in equipartition with the magnetic field). All of these features are consistent with our results on CD instabilities in PFD collimated flows. Pulsar jets, therefore, are one of the strongest cases for a Poynting flux dominated astrophysical flow that has been distorted by current-driven instabilities.

We thank P. E. Hardee for many useful comments and suggestions. M.N. thanks S. Hirose for useful discussions. He is supported, in part, by a National Research Council Resident Research Associateship, sponsored by the National Aeronautics and Space Administration. D.M. is supported, in part, by a NASA Astrophysics Theory Program grant. This research was performed at the Jet Propulsion Laboratory, California Institute of Technology, under contract to NASA. Numerical computations were carried out on Fujitsu VPP5000/32R at the Astronomical Data Analysis Center of the National Astronomical Observatory, Japan. Visualizations were performed on SGI Origin 2000 at the Supercomputing and Visualization Facility of Jet Propulsion Laboratory and on other departmental computers.

## A. THE INITIAL FIELD CONFIGURATION

The initial current-free field is explicitly given by the following formula:

$$\mathbf{B} = (B_x, B_y, B_z) = (B_r \cos \phi - B_\phi \sin \phi, B_r \sin \phi + B_\phi \cos \phi, B_z), \quad (\text{A1})$$

$$B_r \equiv \sum_{n=1}^2 \left\{ \frac{2(z - z_n)}{r \sqrt{(r_n + r)^2 + (z - z_n)^2}} \left( -K(k) + \frac{r_n^2 + r^2 + (z - z_n)^2}{(r_n - r)^2 + (z - z_n)^2} E(k) \right) \right\} \\ \left/ \sum_{n=1}^2 \left\{ \frac{2\pi r_n^2}{(r_n^2 + z_n^2)^{3/2}} \right\} \right., \quad (\text{A2})$$

$$B_\phi \equiv 0, \quad (\text{A3})$$

$$B_z \equiv \sum_{n=1}^2 \left\{ \frac{2}{\sqrt{(r_n + r)^2 + (z - z_n)^2}} \left( K(k) + \frac{r_n^2 - r^2 - (z - z_n)^2}{(r_n - r)^2 + (z - z_n)^2} E(k) \right) \right\} \\ \left/ \sum_{n=1}^2 \left\{ \frac{2\pi r_n^2}{(r_n^2 + z_n^2)^{3/2}} \right\} \right., \quad (\text{A4})$$

$$K(k) = \int_0^{\pi/2} \frac{d\theta}{\sqrt{1 - k^2 \sin^2 \theta}}, \quad E(k) = \int_0^{\pi/2} \sqrt{1 - k^2 \sin^2 \theta} d\theta, \quad (\text{A5})$$

$$k^2 = \frac{4r_n r}{(r_n + r)^2 + z^2}, \quad r \equiv \sqrt{x^2 + y^2}. \quad (\text{A6})$$

On the  $z$ -axis ( $r = 0$ ) we have

$$B_r \equiv 0, \quad (\text{A7})$$

$$B_\phi \equiv 0, \quad (\text{A8})$$

$$B_z \equiv \sum_{n=1}^2 \left\{ \frac{2\pi r_n^2}{\{r_n^2 + (z - z_n)^2\}^{3/2}} \right\} / \sum_{n=1}^2 \left\{ \frac{2\pi r_n^2}{(r_n^2 + z_n^2)^{3/2}} \right\}. \quad (\text{A9})$$

Parameters  $r_n$  and  $z_n$  are the radius and position of the  $n$ th loop (ring) current, respectively, which are set as follows:  $r_n = 1.0$  for all  $n$ , and the positions of pair of current loops are at  $z_n = -3.0$  and  $2z_{\max} + 3.0$ .

## REFERENCES

- Appl, S., & Camenzind, M. 1992, *A&A*, 256, 354
- Appl, S. 1996, *A&A*, 314, 995
- Appl, S., Lery, T., & Baty, H. 2000, *A&A*, 355, 818
- Asada, K., Inoue, M., Uchida, Y., Kamenno, S., Fujisawa, K., Iguchi, S., & Mutoh, M. 2002, *PASJ*, 54, L39
- Bateman, G. 1980, *MHD Instabilities* (Cambridge: MIT Press)
- Baty, H., & Keppens, R. 2002, *ApJ*, 580, 800
- Begelman, M. C., Blandford, R. D., & Rees, M. J. 1980, *Nature*, 287, 307
- Begelman, M. C., Blandford, R. D., & Rees, M. J. 1984, *Rev. Mod. Phys.*, 56, 255
- Begelman, M. C. 1998, *ApJ*, 493, 291
- Benford, G. 1978, *MNRAS*, 183, 29
- Bell, A. R., & Lucek, S. G. 1995, *MNRAS*, 277, 1327
- Birkinshaw, M. 1991, in Hughes P.A., ed., *Beams and Jets in Astrophysics* (Cambridge: Cambridge Univ. Press), p. 278
- Birkinshaw, M., & Worrall, D. M. 1993, *ApJ*, 412, 568

- Blandford, R. D. 1976, MNRAS, 199, 883
- Blandford, R. D. & Znajek, R. L. 1977, MNRAS, 179, 433
- Blandford, R. D. & Payne, D. G. 1982, MNRAS, 199, 883
- Bodo, G., & Ferrari, A. 1982, A&A, 114, 394
- Bodo, G., Rosner, R., Ferrari, A., & Knobloch, E. 1989, ApJ, 341, 631
- Bodo, G., Massaglia, S., Ferrari, A., & Trussoni, E. 1994, A&A, 283, 655
- Bodo, G., Massaglia, S., Rossi, P., Rosner, R., Malagoli, A., & Ferrari, A. 1995, A&A, 303, 281
- Bodo, G., Rosner, R., Ferrari, A., & Knobloch, E. 1996, ApJ, 470, 797
- Bodo, G., Rossi, P., Massaglia, S., Ferrari, A., Malagoli, A., & Rosner, R. 1998, A&A, 333, 1117
- Carvalho, J. C., & O’Dea, C. P. 2002, ApJS, 141, 337
- Carvalho, J. C., & O’Dea, C. P. 2002, ApJS, 141, 371
- Chandrasekhar, S. 1961, Hydrodynamic and Hydromagnetic Stability (New York: Oxford Univ. Press)
- Chiuderi, C., Pietrini, P., & Torricelli-Ciamponi, G. 1989, ApJ, 339, 70
- Cioffi, D. F., & Blondin, J. M. 1992, ApJ, 392, 458
- Clarke, D. A., Norman, M. L., & Burns, J. O. 1986, ApJ, 311, L63
- Clarke, D. A., Harris, D. E., & Carilli, C. L. 1997, 284, 981
- Coburn, W., & Boggs, S. E. 2003, Nature, 423, 415
- Cohn, H. 1983, ApJ, 269, 500
- Colgate, S. A., & Li, H. 1999, ApJS, 264, 357
- Conway, J. E., & Murphy, D. W. 1993, ApJ, 411, 89
- Crutcher, R. M. 1999, ApJ, 520, 706
- Eichler, D. 1993, ApJ, 419, 111
- Eilek, J. A., & Owen, F. N. 2002, ApJ, 567, 202

- Einaudi, G., & Van Hoven, G. 1983, *Sol. Phys.*, 88, 163
- Fendt, C. & Camenzind, M. 1996, *A&A*, 313, 591
- Feretti, L., Perley, R., Giovannini, G., & Andernach, H. 1999, *A&A*, 341, 29
- Ferrari, A., Trussoni, E., & Zaninetti, L. 1981, *MNRAS*, 196, 1051
- Ferrari, A. 1998, *ARA&A*, 36, 539
- Fiedler, R., & Jones, T. W. 1984, *ApJ*, 283, 532
- Freidberg J. P. 1982, *Rev. Mod. Phys.*, 54, 801
- Gill, A. E. 1965, *Phys. Fluids*, 8, 1428
- Gomez, J-L, Marscher, A.P., Alberdi, A., Jorstad, S.G., & Agudo, I. 2001, *ApJ*, 561, L161
- Han, J.-L., & Wielebinski, R. 2002, *Chin. J. Astron. Astrophysics*, 2, 293
- Hardee, P. E. 1979, *ApJ*, 234, 47
- Hardee, P. E. 1983, *ApJ*, 269, 94
- Hardee, P. E., & Norman, M. L. 1988, *ApJ*, 334, 70
- Hardee, P. E., & Clarke, D. A. 1992, *ApJ*, 300, L9
- Hardee, P. E., Cooper, M. A., Norman, M. L., & Stone, J. M. 1992, *ApJ*, 399, 478
- Hardee, P. E., & Clarke, D. A. 1995, *ApJ*, 449, 119
- Hardee, P. E., Clarke, D. A., & Rosen, A. 1997, *ApJ*, 485, 533
- Hardee, P. E., & Stone, J. M. 1997, *ApJ*, 483, 121
- Hardee, P. E., & Rosen, A. 1999, *ApJ*, 524, 650
- Hardee, P. E., & Rosen, A. 2002, *ApJ*, 576, 204
- Hester, J. J. et al. 2002, *ApJ*, 577, L49
- Heyvaerts, J., & Norman, C. 2003, *ApJ*, 596, 1240
- Heyvaerts, J., & Norman, C. 2003, *ApJ*, 596, 1256
- Heyvaerts, J., & Norman, C. 2003, *ApJ*, 596, 1270

- Hood, A. W., & Priest, E. R. 1979, *Sol. Phys.*, 64, 303
- Hummel, C. A., et al. 1992, *A&A*, 257, 489
- Hutchison, J. M., Cawthorne, T. V., & Gabuzda, D. C. 2001, *MNRAS*, 321k, 525
- Jones D. L., et al. 1996, *ApJ*, 466, L63
- Kadomtsev, B. B., 1966, *Rev. Plasma Phys.*, 2, 153
- Kersalé, E., Longaretti, P.-Y., & Pelletier, G. 2000 *A&A*, 363, 1166
- Koide, S., Nishikawa, K.-I., & Mutel, R. L. 1996, *ApJ*, 463, L71
- Koide, S., Shibata, K., Kudoh, T., & Meier, D. L. 2002, *Science*, 295, 1688
- Komissarov, S. S. 1999, *MNRAS*, 308, 1069
- Kössl, D., & Müller, E. 1988, *aap*, 206, 204
- Kössl, D., Müller, E., & Hillebrandt, W. 1990, *A&A*, 229, 378
- Krasnopolsky, R., Li, Z.-Y., & Blandford, R. 1999, *ApJ*, 526, 631
- Krause, M., & Camenzind, M. 2001, *A&A*, 380, 789
- Krause, M. 2003, *A&A*, 398, 113
- Krause, M., & Löhr, A. 2004, *A&A*, accepted (astro-ph/0403143)
- Krichbaum, T. P., Hummel, C. A., Quirrenbach, A., Schalinski, C. J., Witzel, A., Johnson, K. J., Muxlow, T. W. B., & Qian, S. J. 1990, *A&A*, 230, 271
- Krichbaum, T. P., et al. 1992, *A&A*, 260, 33
- Krichbaum, T. P., Alef, W., Witzel, A., Zensus, J. A., Booth, R. S., Greve, A., & Rogers, A. E. E. 1998, *A&A*, 329, 873
- Kronberg, P. P. 1994, *Rep. Prog. Phys.*, 57, 325
- Kruskal, M. D., Johnson, J. L., Gottlieb, M. B., & Goldman, L. M. 1958, *Phys. Fluids*, 1, 421
- Kulsrud, R. M., & Andersen, S. W., 1992, *ApJ*, 396, 606
- Landau, L. D., & Lifshitz, E. M. 1959, *Course of Theoretical Physics: Fluid Mechanics (Vol. 6; Oxford: Pergamon Press)*

- Lapidus, A. 1967, *J. Comput. Phys.*, 2, 154
- Lery, T., Baty, H., & Appl, S. 2000, *A&A*, 355, 1201
- Lery, T., & Frank, A. 2000, *ApJ*, 533, 897
- Li, Z.-Y., Begelman, M. C., & Chiueh, T. 1992, *ApJ*, 384, 567
- Li, L.-X. 2000, *ApJ*, 531, L111
- Li, H., Lovelace, R. V. E., Finn, J. M., & Colgate, S. 2001, *ApJ*, 561, 915
- Lind K. R., Payne, D. G., Meier, D. L., & Blandford, R. D. 1989, *ApJ*, 344, 89
- Levinson, A. 1998, *ApJ*, 507, 145
- Lobanov, A. P., & Zensus, J. A. 2001, *Science*, 294, 128
- Longaretti, P.-Y. 2003, *Phys. Lett. A*, 320, 215
- Lovelace, R. V. E. 1976, *Nature*, 262, 649
- Lovelace, R. V. E., Wang, J. C. L., & Sulkanen, M. E. 1987, *ApJ*, 315, 504
- Lovelace, R. V. E., Li, H., Koldoba, A. V., Ustyugova, G. V., & Romanova, M. M. 2002, *ApJ*, 572, L445
- Lovelace, R. V. E., & Romanova, M. M. 2003, *ApJ*, 596, L159
- Lynden-Bell, D. 1996, *MNRAS*, 279, 389
- Lyubarskii, Yu. E. 1999, *MNRAS*, 308, 1006
- Mantovani, F., Junor, W., Valerio, C., & McHardy, I. 1999, *A&A*, 346, 397
- Massaglia, S., Bodo, G., & Ferrari, A. 1996, *A&A*, 307, 997
- Matsumoto, R., Uchida, Y., Hirose, S., Shibata, K., Hayashi, M. R., Ferrari, A., Bodo, G., & Norman, C. 1996, *ApJ*, 461, 115
- Meier, D. L., Edgington, S., Godon, P., Payne, D. G., & Lind K. R. 1997, *Nature*, 388, 350
- Meier, D. L., Koide, S., & Uchida, Y. 2001, *Science*, 291, 84
- Micono, M., Bodo, G., Massaglia, S., Rossi, P., Ferrari, A., & Rosner, R. 2000, *A&A*, 360, 795
- Murphy, D. W., et al. 1999, *New Astronomy Reviews*, 43, 727

- Mori, K., Burrows, D. N., Pavlov, G. G., Hester, J. J., Shibata, S., & Tsunemi, H. 2004, in *Young Neutron Stars and Their Environments IAU Symposium, Vol. 218*, ed. F. Camilo & B. M. Gaensler (astro-ph/0311409)
- Mouschovias, T. 1976, *ApJ*, 297, 141
- Nakamura, M., Uchida, Y., & Hirose, S. 2001, *New Astronomy*, 6, 61
- Narayan, R., Mahadevan, R., & Quataert, E. 1998, in *Theory of Black Hole Accretion Disks*, ed. M.A. Abramowicz, G. Bjornsson, & J.E. Pringle, Cambridge Univ. Press, p. 148
- Norman, M. L., Smarr, L., Winkler, K.-H. A., & Smith, M. D. 1982, *A&A*, 113, 285
- Norman, M. L., & Hardee, P. E. 1988, *ApJ*, 334, 80
- Ostriker, E. C. 1997, *ApJ*, 486, 291
- Ouyed, R., & Pudritz, R. E. 1997a, *ApJ*, 482, 712
- Ouyed, R., & Pudritz, R. E. 1997b, *ApJ*, 484, 794
- Ouyed, R., & Pudritz, R. E. 1999, *MNRAS*, 309, 233
- Ouyed, R., Clarke, D. A., & Pudritz, R. E. 2003, *ApJ*, 582, 292
- Owen, F. N., Hardee, P. E., & Cornwell, T. J. 1989, *ApJ*, 340, 698
- Pavlov, G. G., Teter, M. A., Kargaltsev, O., & Sanwai, D. 2003, *ApJ*, 591, 1157
- Payne, D. G., & Cohn, H. 1985, *ApJ*, 291, 655
- Perley, R. A., Bridle, A. H., & Willis, A. G. 1984, *ApJS*, 54, 291
- Perlman, E. S., Biretta, J. A., Zhou, F., Sparks, W. B., Macchetto, F. D. 1999, *AJ*, 117, 2185
- Potash, R. I., & Wardle, J. F. C. 1980, *ApJ*, 239, 42
- Ray, T. P. 1981, *MNRAS*, 196, 195
- Romanova, M. M., & Lovelace, R. V. E. 1998, *ApJ*, 475, 97
- Romanova, M. M., Ustyugova, G. V., Koldoba, A. V., Chechetkin, V. M., & Lovelace, R. V. E. 1998, *ApJ*, 500, 703
- Roos, N., Kaastra, J. S., & Hummel, C. A. 1993, *ApJ*, 409, 130

- Rosen, A., Hardee, P. E., Clarke, D. A., Johnson, A. 1999, *ApJ*, 510, 136
- Rosen, A., & Hardee, P. E. 2000, *ApJ*, 542, 750
- Rubin, E. L., & Burstein, S. Z. 1967, *J. Comput. Phys.*, 2, 178
- Shafranov, V. D. 1957, *Sov. Phys.–JETP*, 6, 545
- Scott, E. H., & Black, D. C. 1980, *ApJ*, 239, 166
- Shibata, K. 1983, *PASJ*, 35, 263
- Shibata, K., & Uchida, Y. 1985, *PASJ*, 37, 31
- Shibata, K., & Uchida, Y. 1986, *PASJ*, 38, 631
- Spruit, H. C., Foglizzo, T., & Stehle, R. 1997, *MNRAS*, 288, 333
- Stirling, A. M., et al. 2003, *MNRAS*, 341, 405
- Stone, J. M., Xu, J., & Hardee, P. E. 1997, *ApJ*, 483, 136
- Todo, Y., Uchida, Y., Sato, T., & Rosner, R. 1992, *PASJ*, 44, 245
- Todo, Y., Uchida, Y., Sato, T., & Rosner, R. 1993, *ApJ*, 403, 164
- Tomimatsu, A., Matsuoka, T., & Takahashi, M. 2001, *Phys. Rev. D*, 64, 123003
- Tomisaka, K. 1996, *PASJ*, 48, 701
- Uchida, Y., & Shibata, K. 1985, *PASJ*, 37, 515
- Uchida, Y., & Shibata, K. 1986, *Can. J. Phys.*, 64, 507
- Uchida, Y., Todo, Y., Rosner, R., & Shibata, K. 1992, *PASJ*, 44, 227
- Ustyugova, G. V., Koldoba, A. V., Romanova, M. M., Chechetkin, V. M., & Lovelace, R. V. E. 1995, *ApJ*, 439, L39
- Ustyugova, G. V., Koldoba, A. V., Romanova, M. M., Chechetkin, V. M., & Lovelace, R. V. E. 2000, *ApJ*, 541, L21
- Vlahakis, N. & Königl, A. 2001, *ApJ*, 563, L129
- Vlahakis, N. 2003, *New Astronomy Rev.*, 47, 701
- Vlahakis, N. & Königl, A. 2003a, *ApJ*, 596, 1080

Vlahakis, N. & Königl, A. 2003b, ApJ, 596, 1104

Vlahakis, N. & Königl, A. 2004, ApJ, 605, 656

Wang, D.-X., Ma, R.-Y., Lei, W.-H., & Yao, G.-Z. 2004, ApJ, 601, 1031

Xu, J., Hardee, P. E., & Stone, J. M. 2000, ApJ, 543, 161

Zhao, J-H., Burns, J. O., Hardee, P. E., & Norman, M. L. 1992a, ApJ, 387, 69

Zhao, J-H., Burns, J. O., Norman, M. L., & Sulkanen, M. E. 1992b, ApJ, 387, 83

Zensus, J.A., Cohen, M.H., & Unwin, S.C. 1995, ApJ, 443, 35

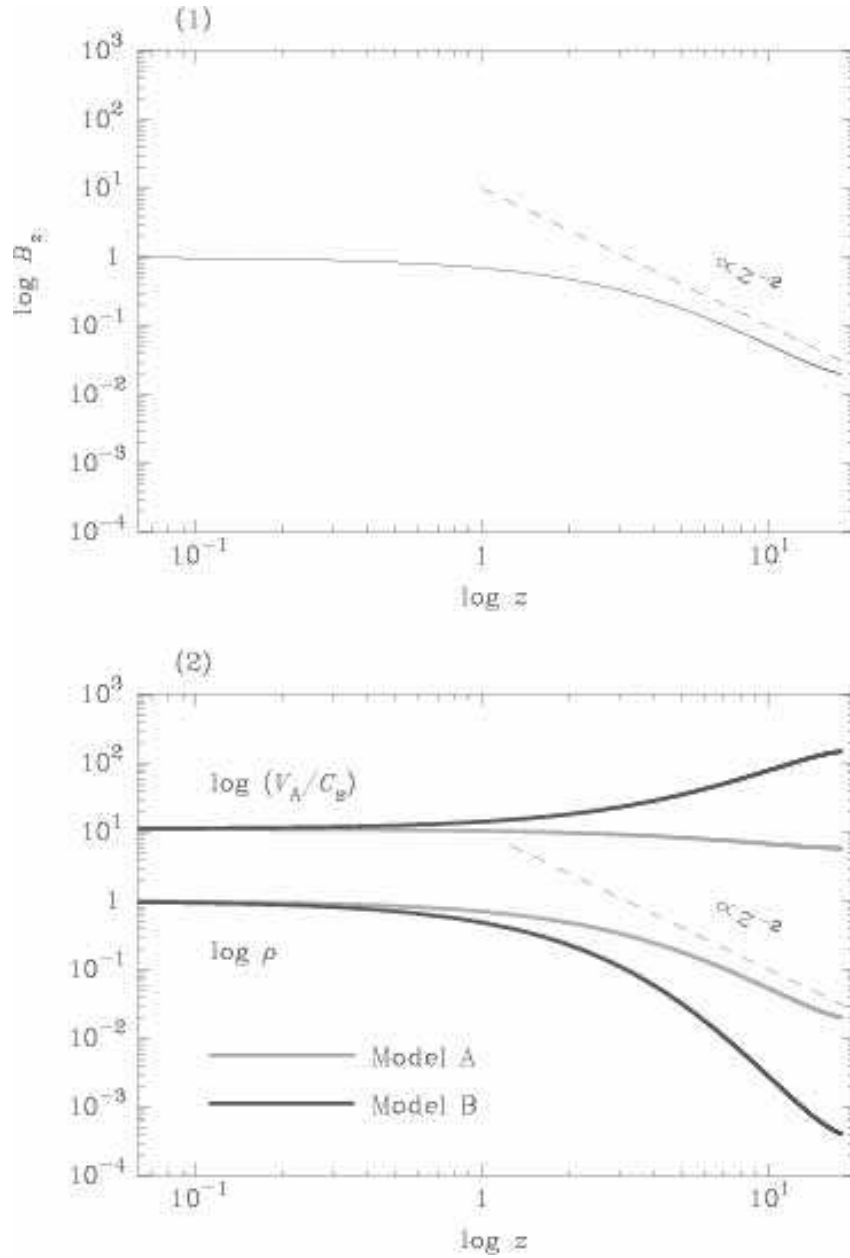


Fig. 1.— Initial profiles along the  $z$ -axis of (1) the axial component of the magnetic field  $B_z$  for all models and (2) density  $\rho$  and ratio of Alfvén velocity to sound velocity  $V_A/C_s$  in logarithmic scale for models A (*light gray solid line*) and B (*dark gray solid line*). The broken line indicates a  $z^{-2}$  power law variation for comparison.

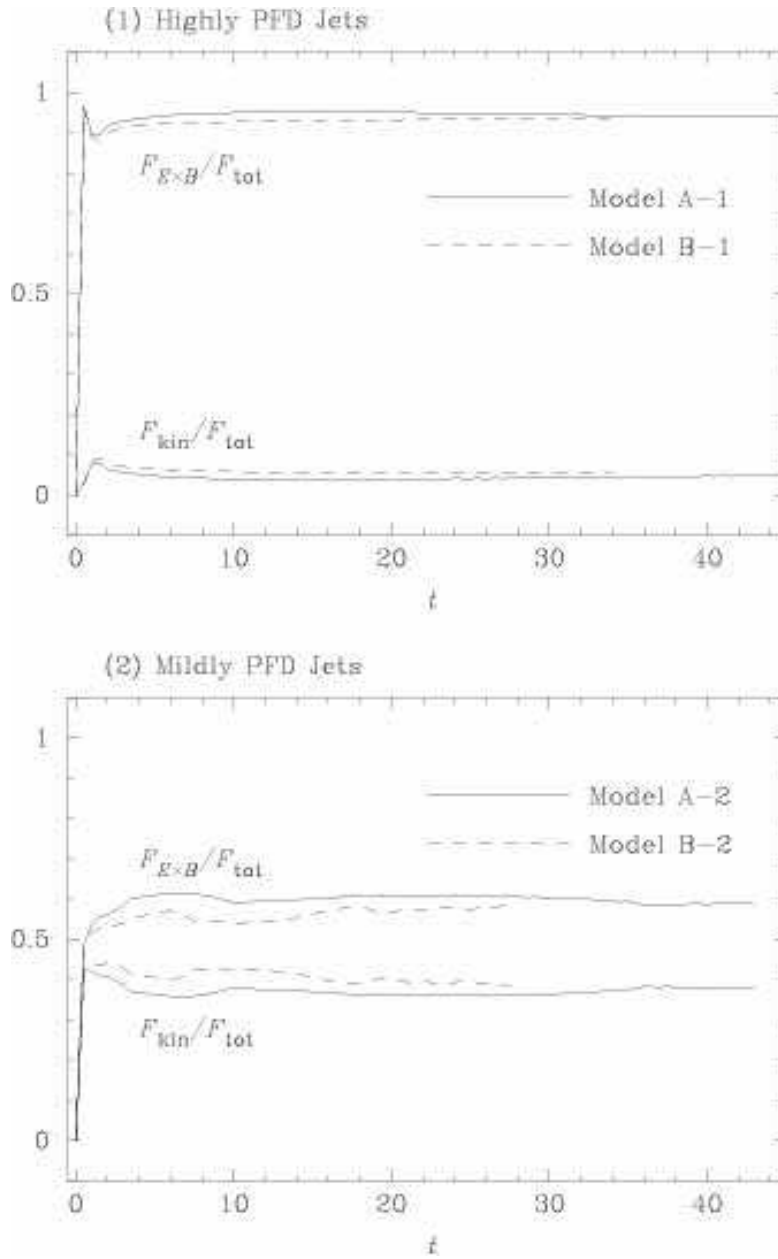


Fig. 2.— Time variation of the energy fluxes injected through the  $z = 0$  plane. Kinetic energy flux  $F_{\text{kin}}$  and Poynting flux  $F_{E \times B}$  are normalized by the total energy flux  $F_{\text{tot}} = F_{\text{kin}} + F_{E \times B} + F_{\text{th}}$  (thermal energy flux). Both Case 1 (*Highly PFD Jets*) and Case 2 (*Mildly PFD Jets*) are shown. The solid line shows Model A (*slowly decreasing ambient density*) and the broken line Model B (*steeply decreasing ambient density*).

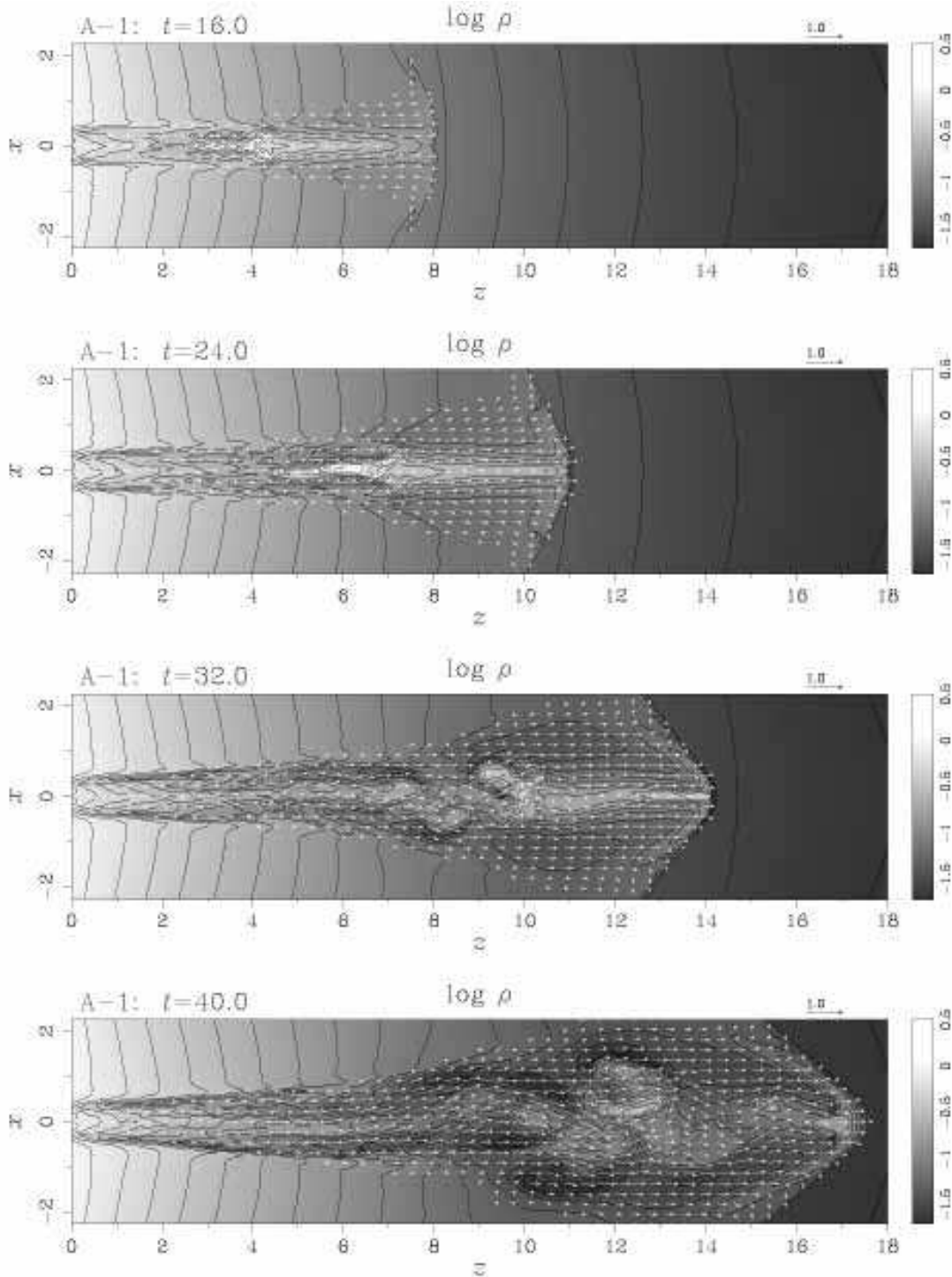


Fig. 3.— Time evolution of the region ( $|x| \leq 2.25$ ,  $0.0 \leq z \leq 18.0$ ) for Model A - 1. Contour images of the density distribution (logarithmic scale) are shown along with the poloidal velocity field in the  $x - z$  plane. Model times are given at upper left in each of the four panels. The length of the arrow at upper right in each panel shows the unit velocity.

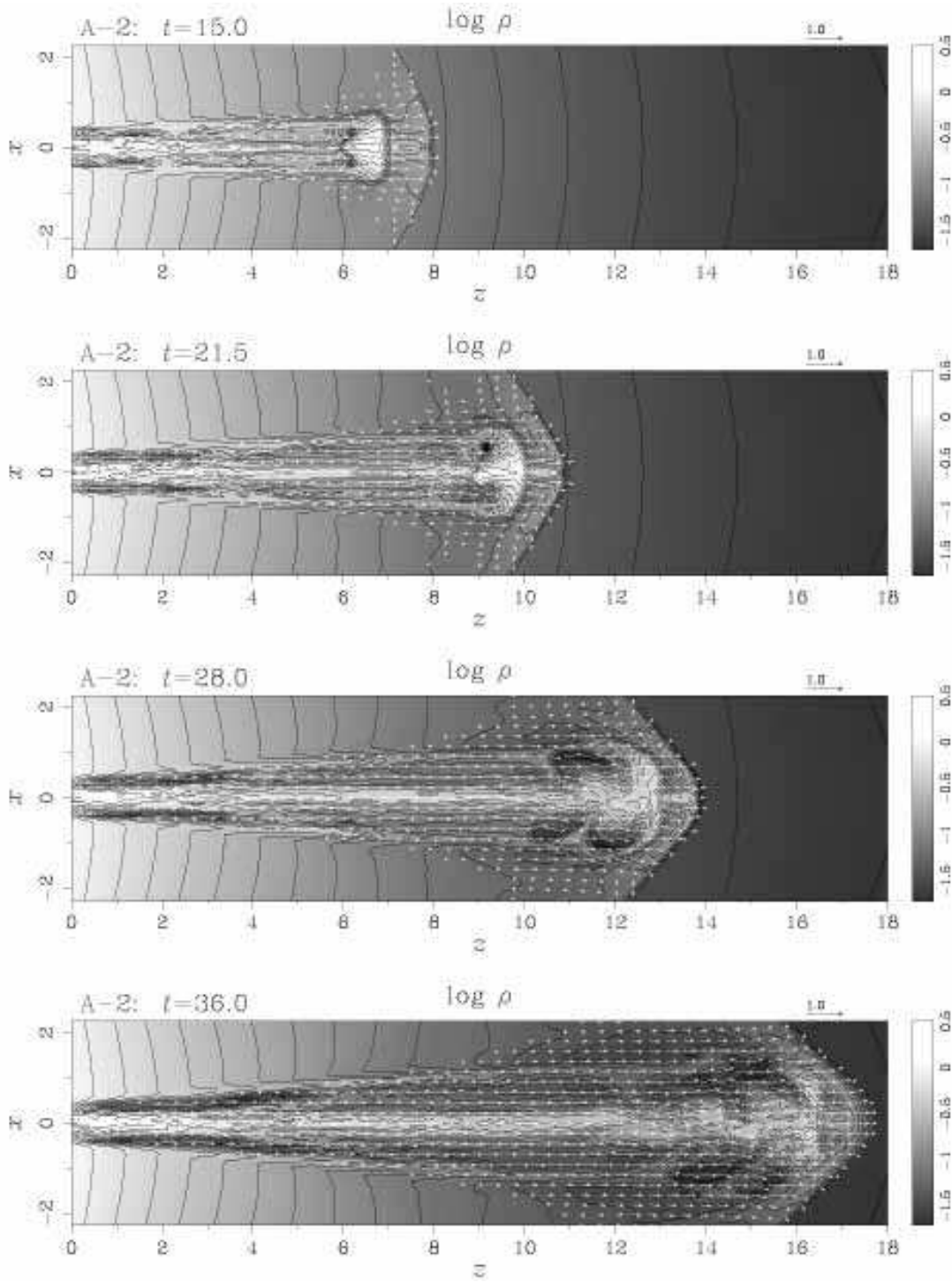


Fig. 4.— Similar to Fig. 3, but for Model A - 2.

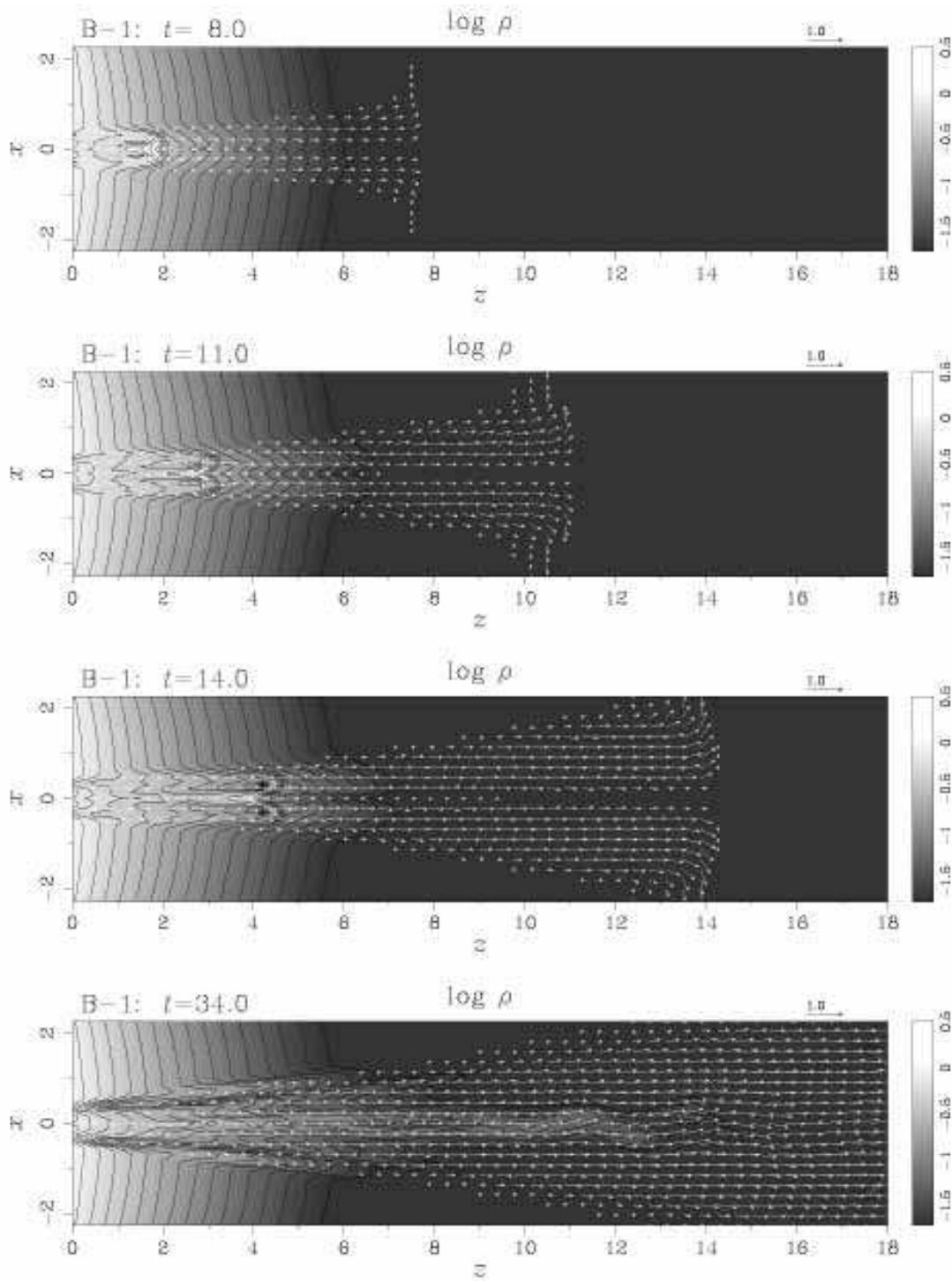


Fig. 5.— Similar to Fig. 3, but for Model B - 1.

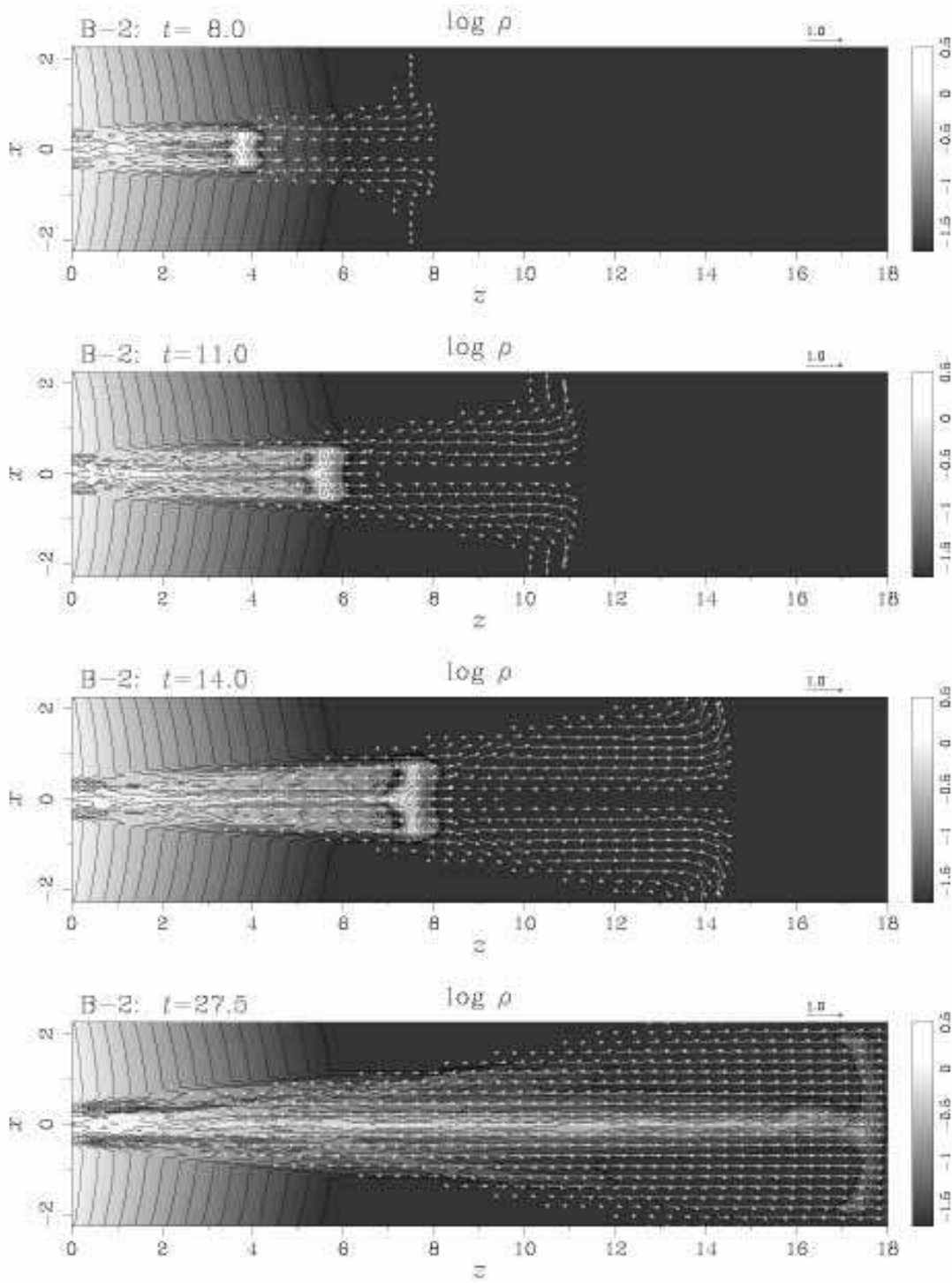


Fig. 6.— Similar to Fig. 3, but for Model B - 2.

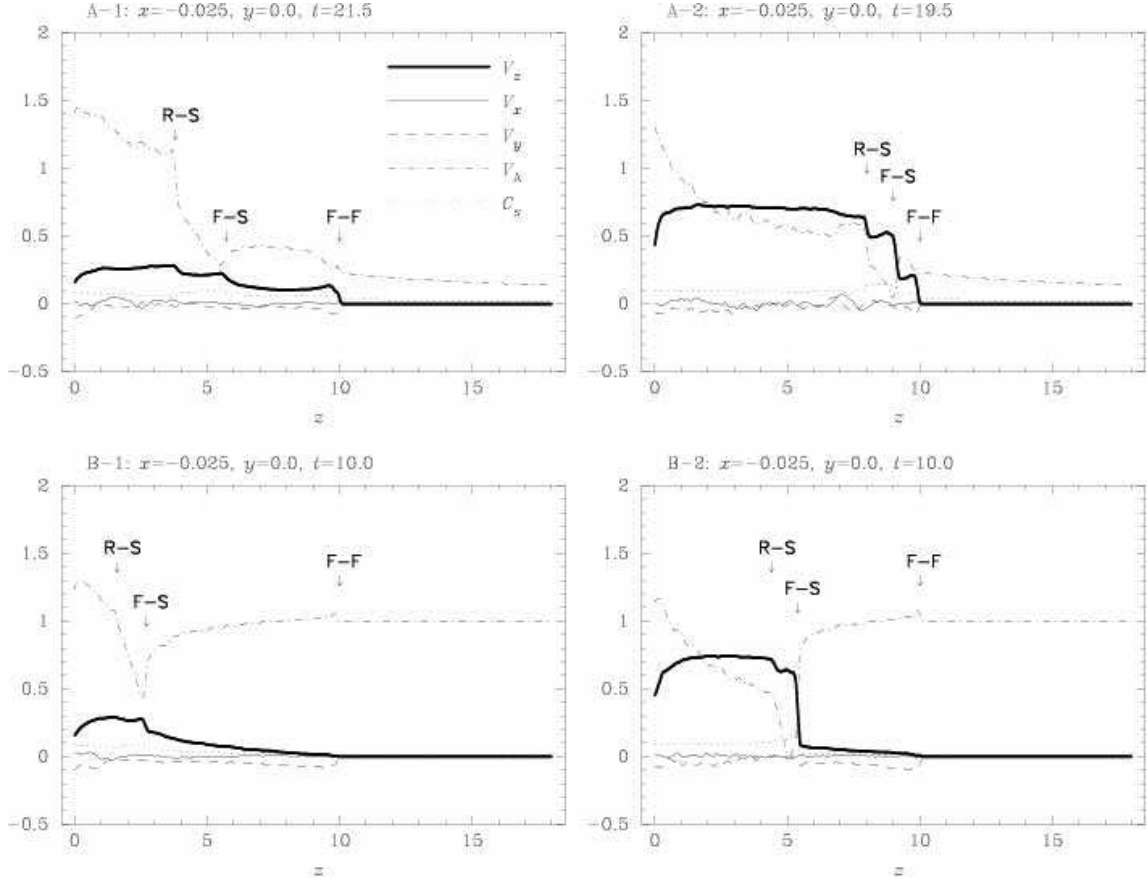


Fig. 7.— Offset axial velocity profiles parallel the  $z$ -axis at  $(x, y) = (-0.025, 0.0)$  in the intermediate stage for each of the models. Shown are the components of velocity ( $V_x, V_y, V_z$ ) and the local  $V_A$  and  $C_s$  at model times  $t = 21.5$  (*Upper-Left: A - 1*),  $t = 19.5$  (*Upper-Right: A - 2*),  $t = 10.0$  (*Lower-Left: B - 1*), and  $t = 10.0$  (*Lower-Right: B - 2*). The labels F-F, F-S, and R-S indicate the positions of the forward fast-mode, forward slow-mode, and reverse slow-mode compressive MHD (magnetosonic) waves, respectively. Some of these will steepen into MHD shock waves during the dynamical evolution. Each time selected corresponds to when the F-F compressive/shock wave fronts reach approximately  $z = 10.0$ .

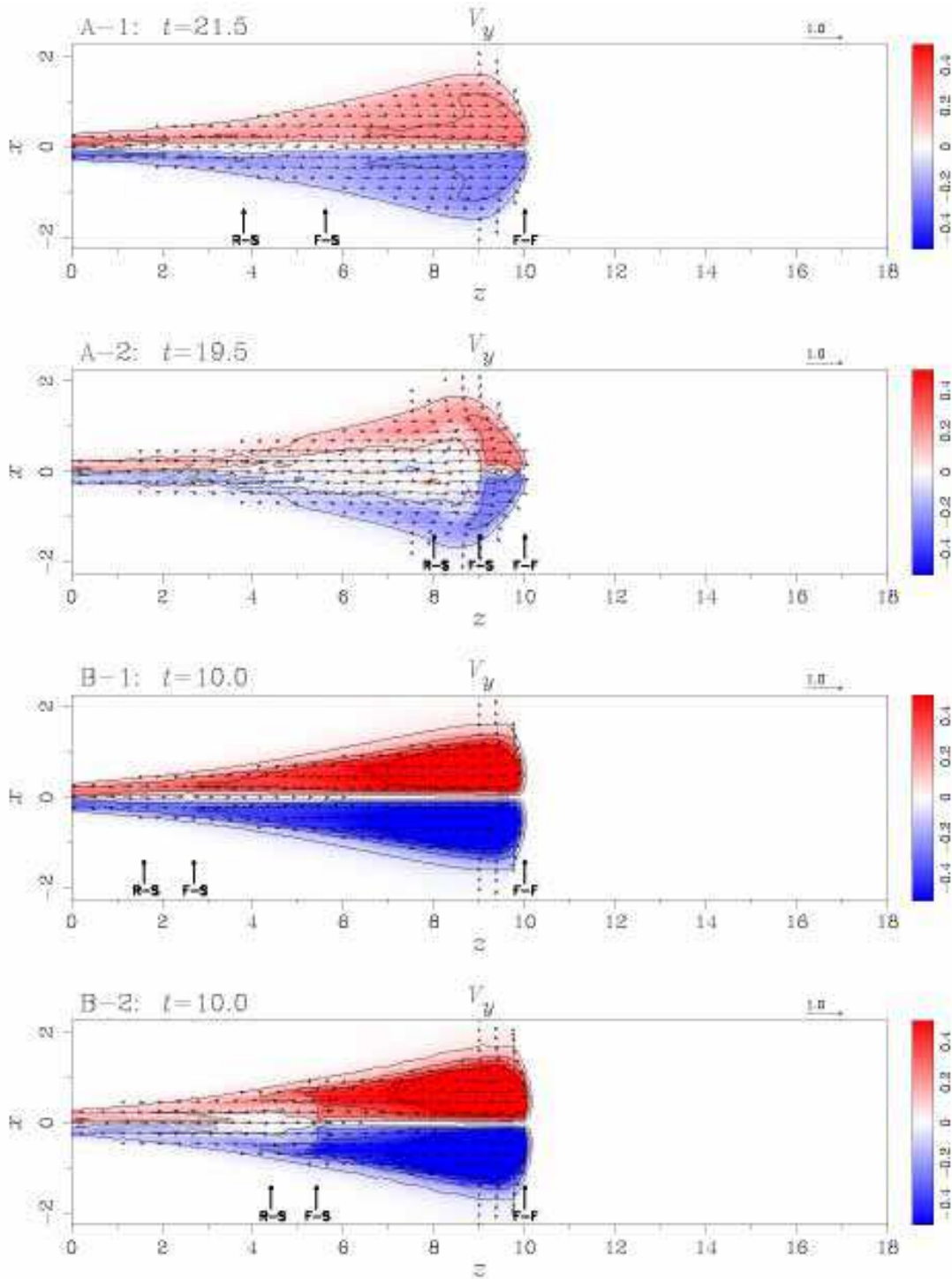


Fig. 8.— Snapshots of the azimuthal velocity  $V_y$  in the intermediate stage for each of the models. The labels F–F, F–S, and R–S are the same as those in figure 7.

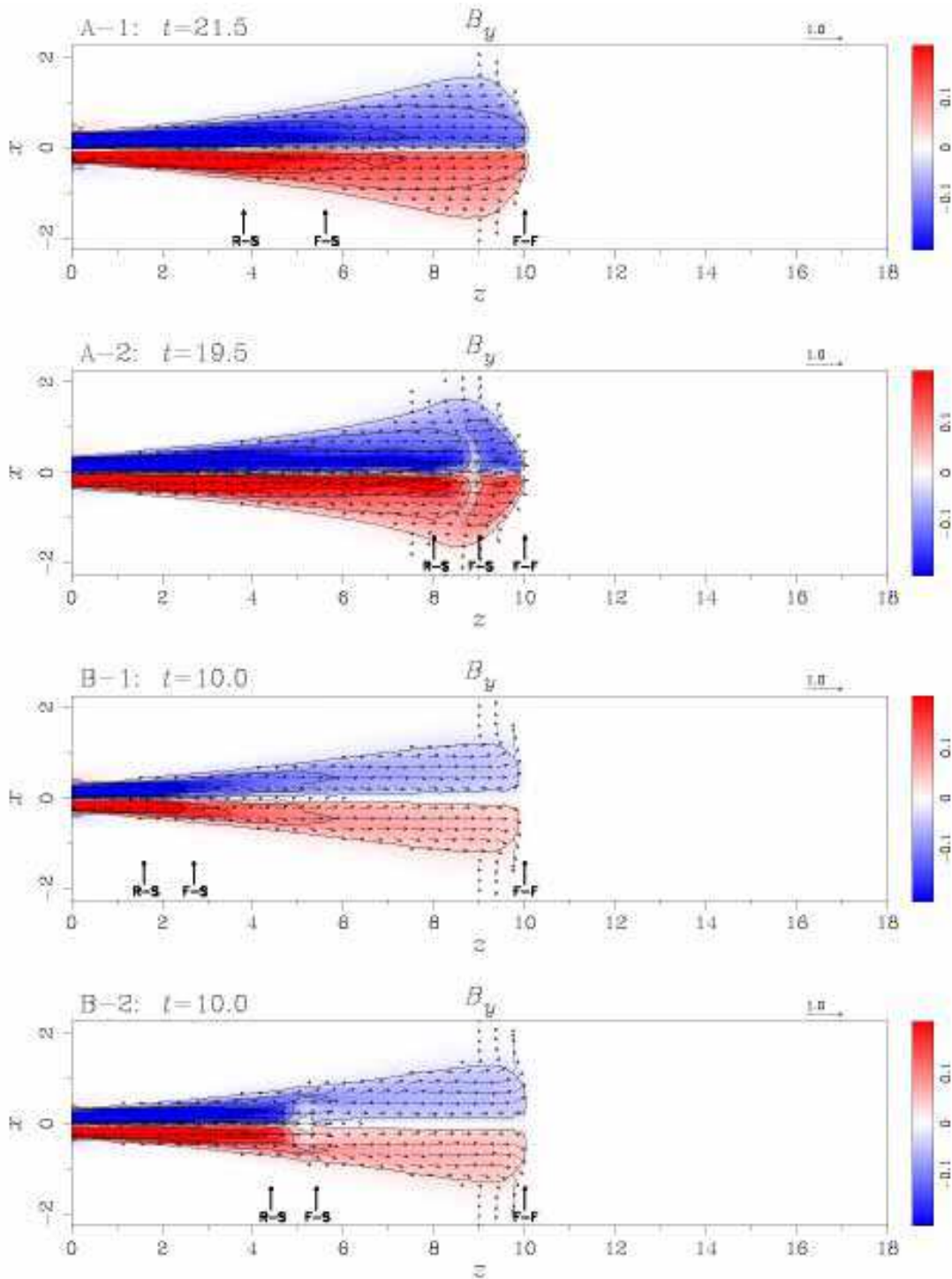


Fig. 9.— Similar to figure 8, but for  $B_y$ .

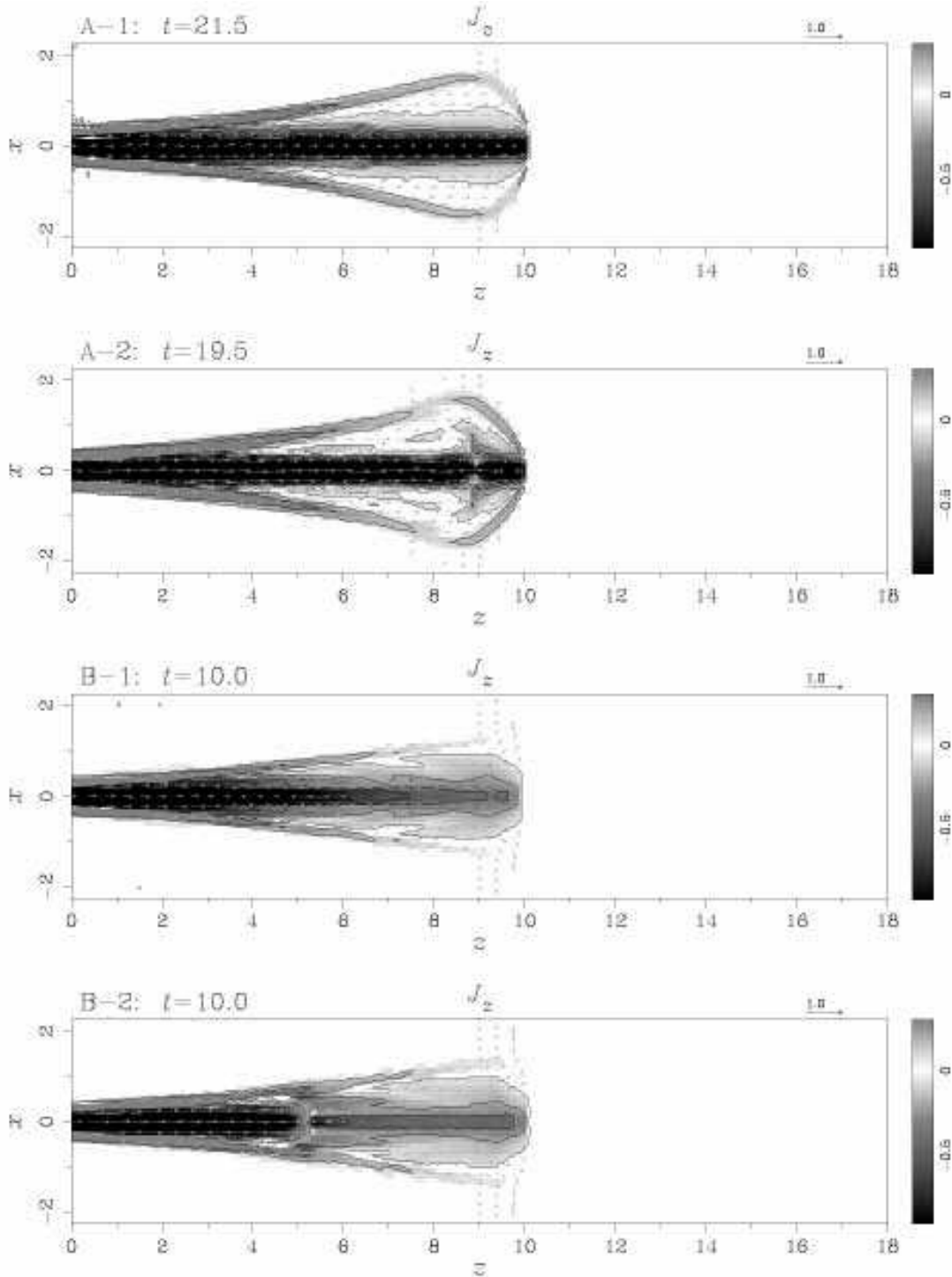


Fig. 10.— Snapshots of the axial current density  $J_z$  in the intermediate stage for each of the models. The figures show a closed circulating current system, in which one current path occurs near the central ( $z$ ) axis and co-moves with the PFD jet ( $\mathbf{J}^c$ ), while the other conically-shaped current returns outside ( $\mathbf{J}^{rc}$ ).

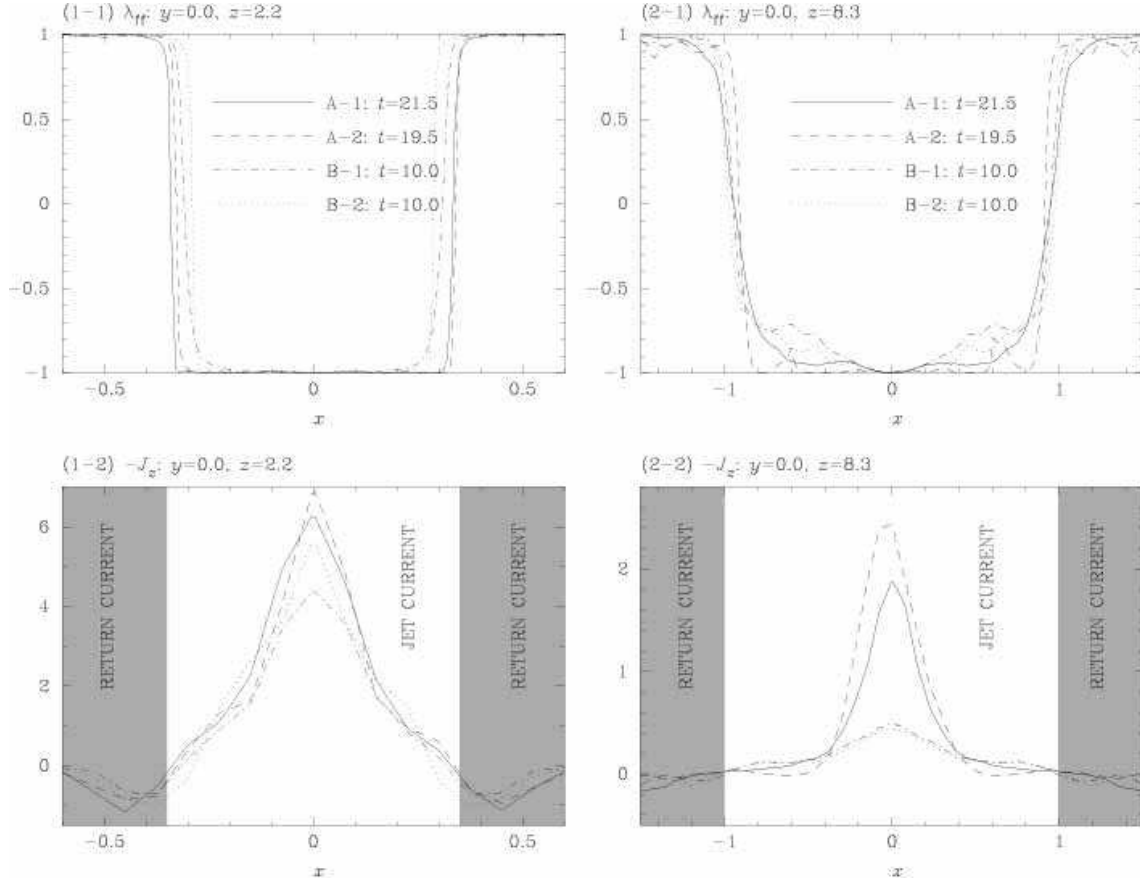


Fig. 11.— Transverse profiles parallel to the  $x$ -axis of the force-free parameter  $\lambda_{ff}$  (*Upper*) and of the negative of the axial current density  $-J_z$  (*Lower*) in the intermediate stage. Two axial positions are shown:  $z = 2.2$  (*Left*) and  $z = 8.3$  (*Right*).  $|\lambda_{ff}| = 1$  indicates that  $\mathbf{J}$  is parallel or anti-parallel to the local  $\mathbf{B}$  direction (*i.e.*, force-free). The reversal of the sign of  $\lambda_{ff}$  from -1 to 1 (seen in the *Upper* panels) indicates a change in sign of the current flow from  $\mathbf{J}^{jc}$  to  $\mathbf{J}^{rc}$  (light gray colored regions seen in both *Lower* panels).

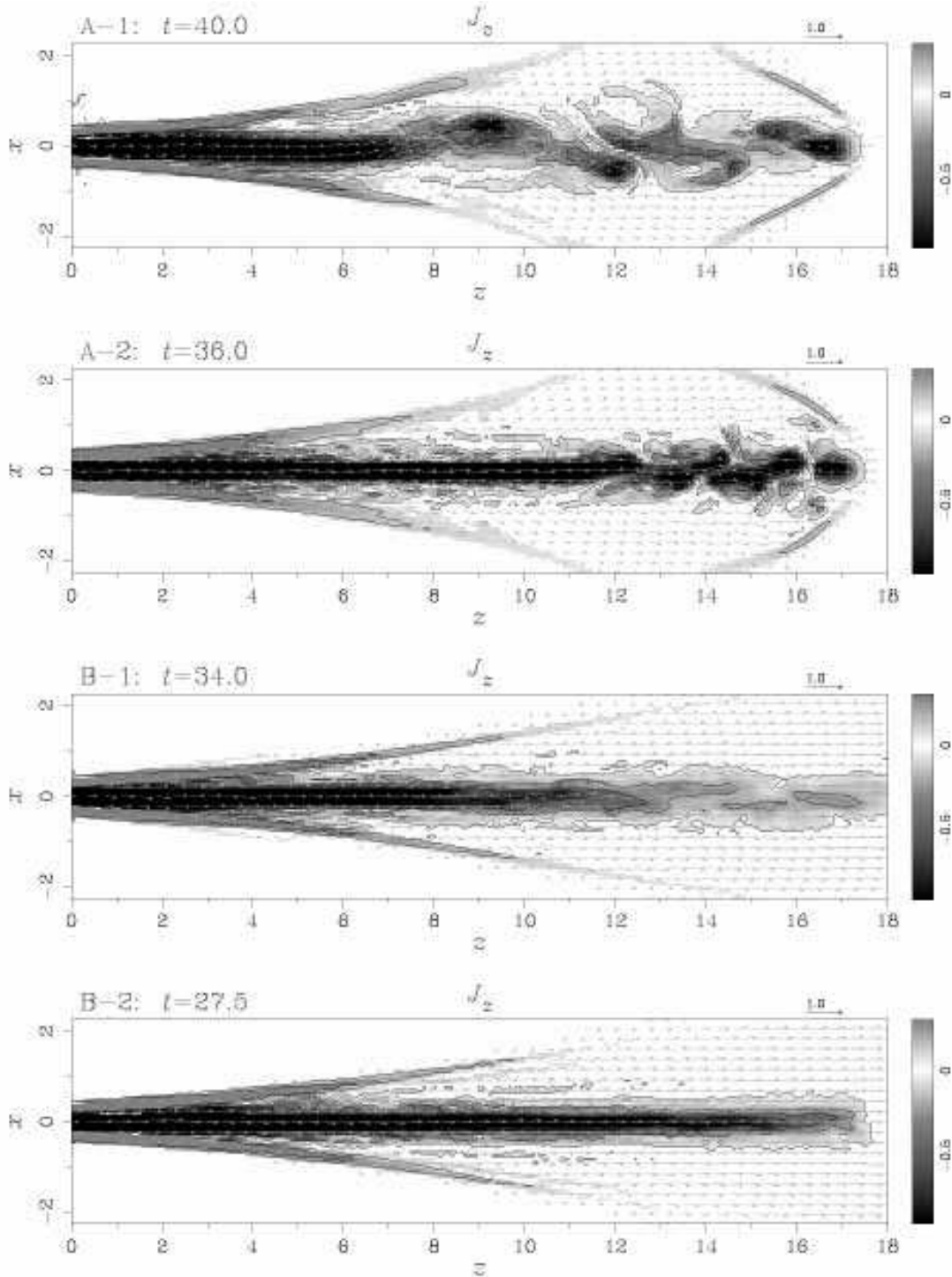


Fig. 12.— Snapshots of the axial current density  $J_z$  in the final stage for each of the models. Each time selected corresponds to when the F–F (A – 1 and A – 2) or the F–S (B – 1 and B – 2) shock wave fronts approach or exceed approximately  $z = 18.0$ . Note that these figures are 2-D meridional slices only through the 3-D jet structure. While the distributions of  $\mathbf{J}^c$  appear asymmetric in models A – 1, A – 2, and B – 1, the actual jet structures in these models are a three-dimensional spiral helix.

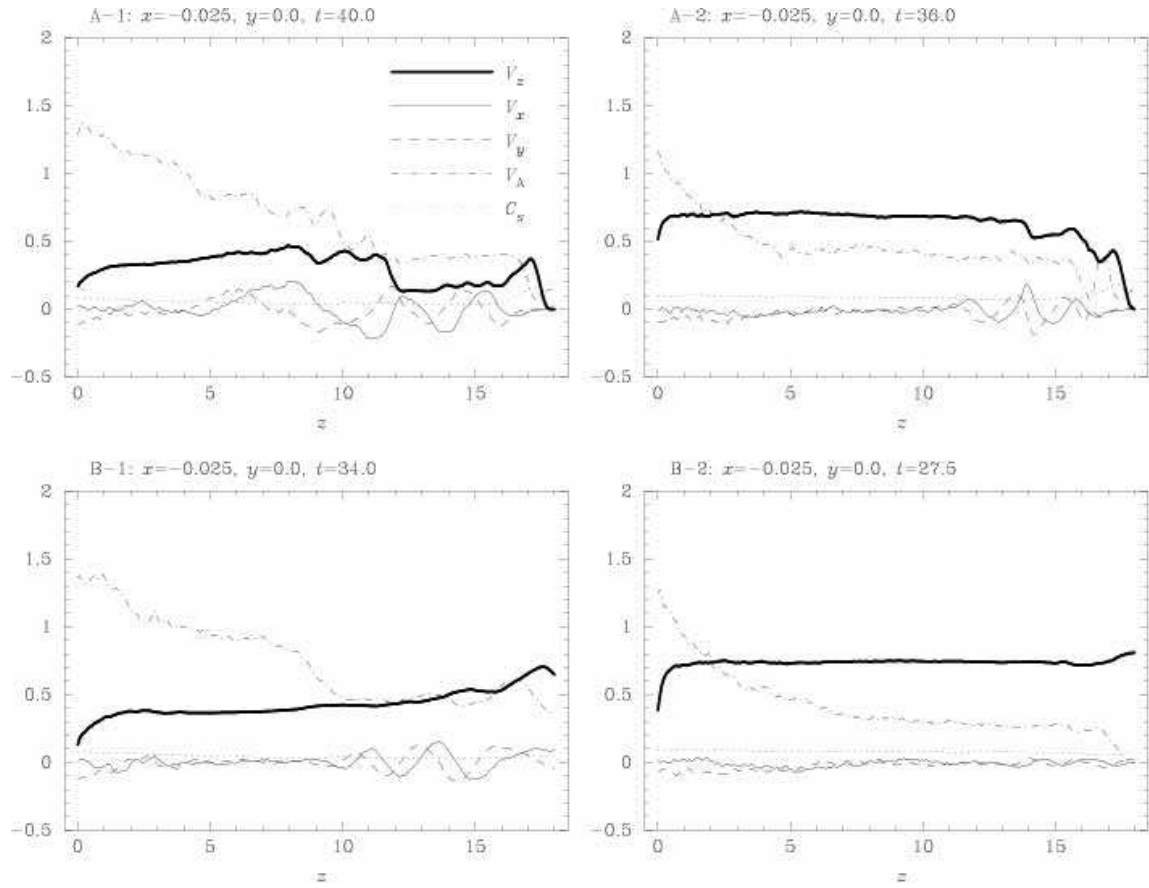


Fig. 13.— Similar to figure 7, but for the final stage in each of the models.

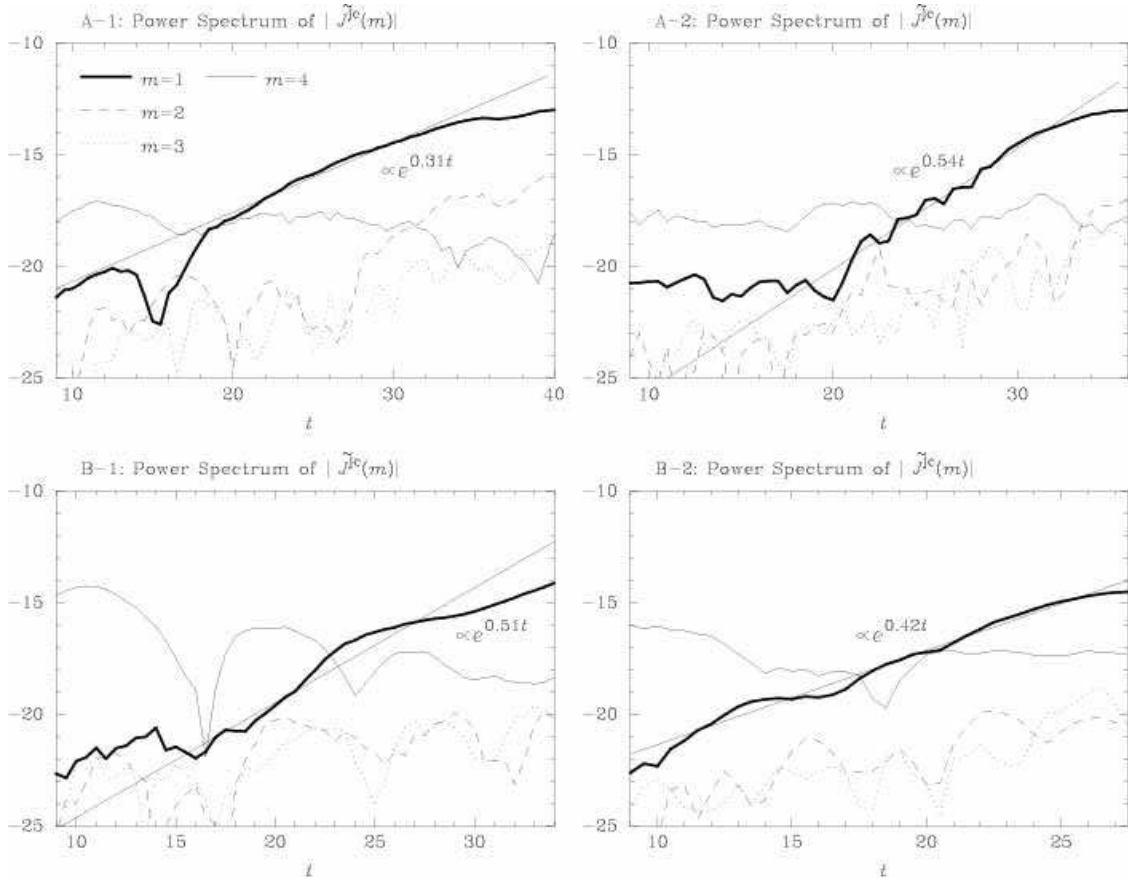


Fig. 14.— Growth of unstable CD modes for each model sequence, showing the time variation of the azimuthal Fourier power in modes  $m = 1 - 4$ , on a natural log scale. Solid lines are derived by fitting the slopes of the  $m = 1$  mode growth to a linear function.

A-1:  $x = -0.025, y = 0.0$

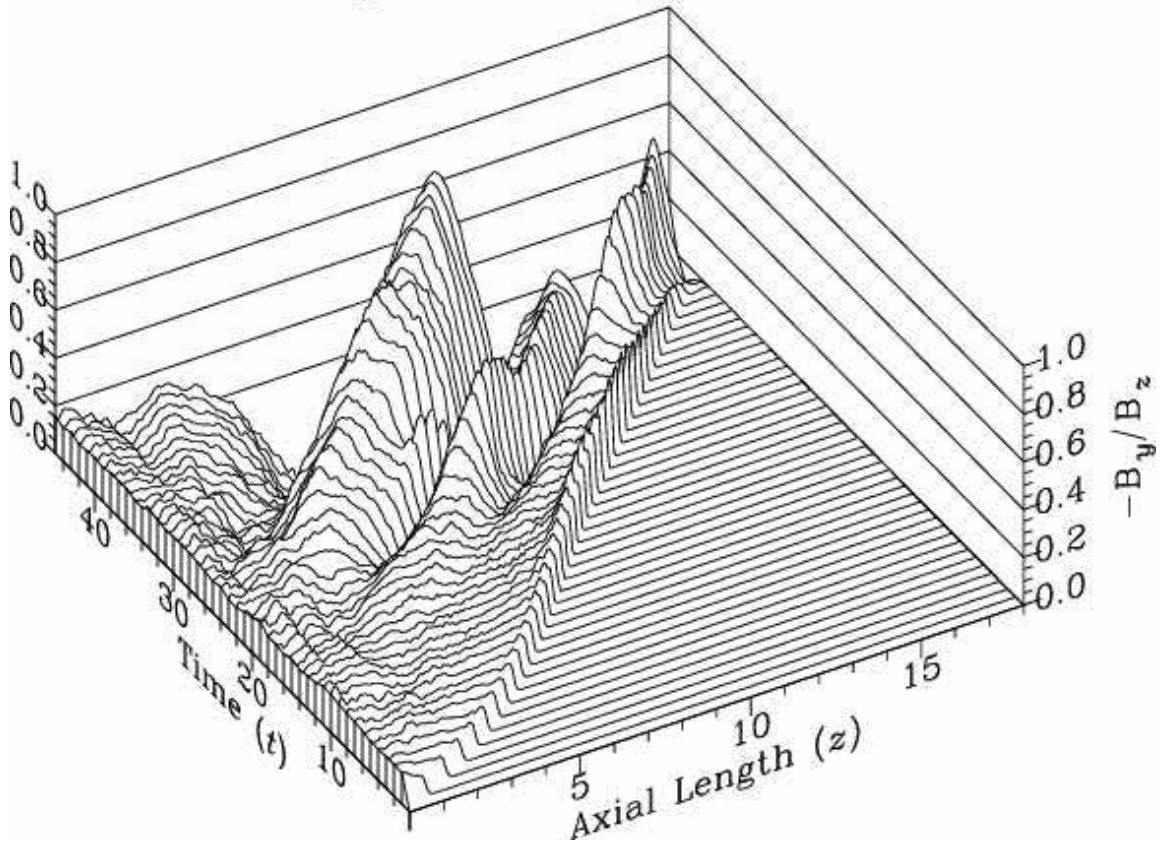


Fig. 15.— Space-time diagram showing the growth of the ratio of transverse and axial magnetic field  $-B_y/B_z$  during the interval  $t = 0.0 - 45.0$ . Values are measured near, and parallel to, the  $z$  axis ( $x = -0.025, y = 0.0$ ) for Model A - 1.

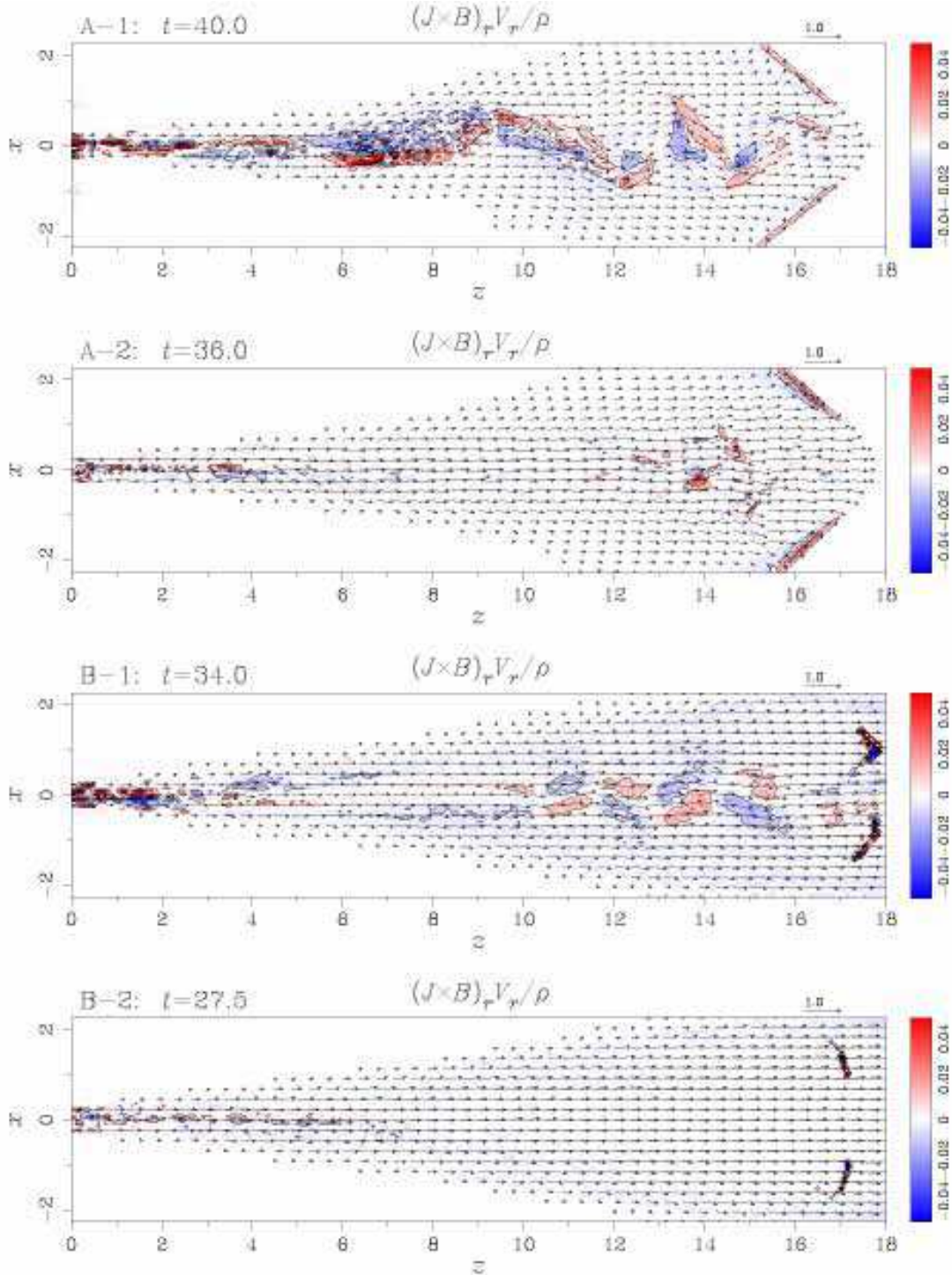
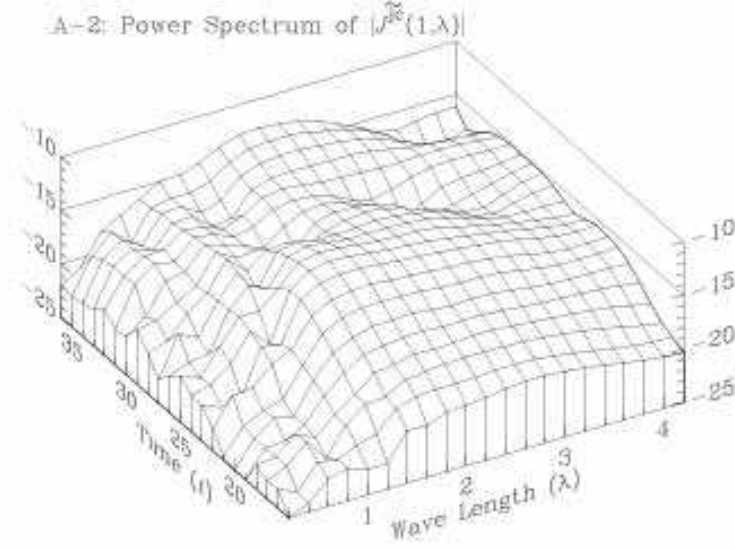
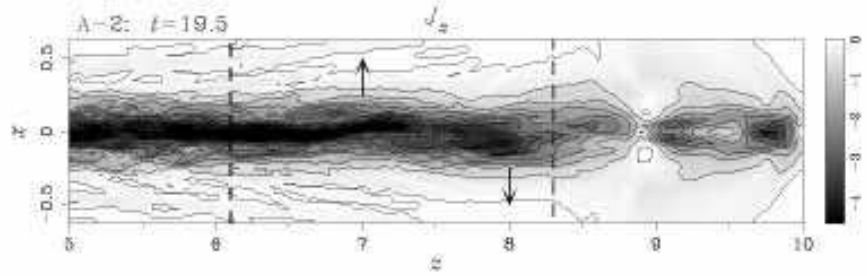


Fig. 16.— Snapshots of the radial specific power generated by the Lorentz force  $(\mathbf{J} \times \mathbf{B})_r V_r / \rho$  in the final stage for each of the models. The  $r$ -component of the Lorentz force is composed of both (i) the magnetic pressure gradient of the azimuthal and axial components  $-(\partial/\partial r)[(B_\phi^2 + B_z^2)/2]$  and of (ii) the hoop-stress  $-B_\phi^2/r$ . Positive power (*Red*) indicates the net acceleration (increase in radial velocity); negative power (*Blue*) indicates net deceleration. There is a strong correlation between the power distribution and the wiggled structures seen in models A – 1, A – 2, and B – 1.

(1)



(2)



(3)

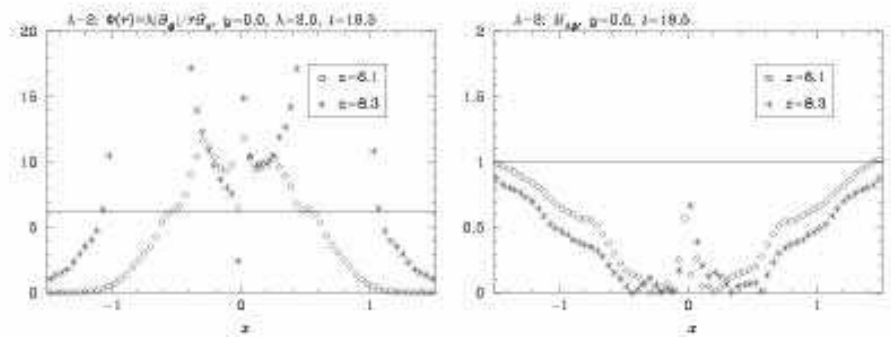
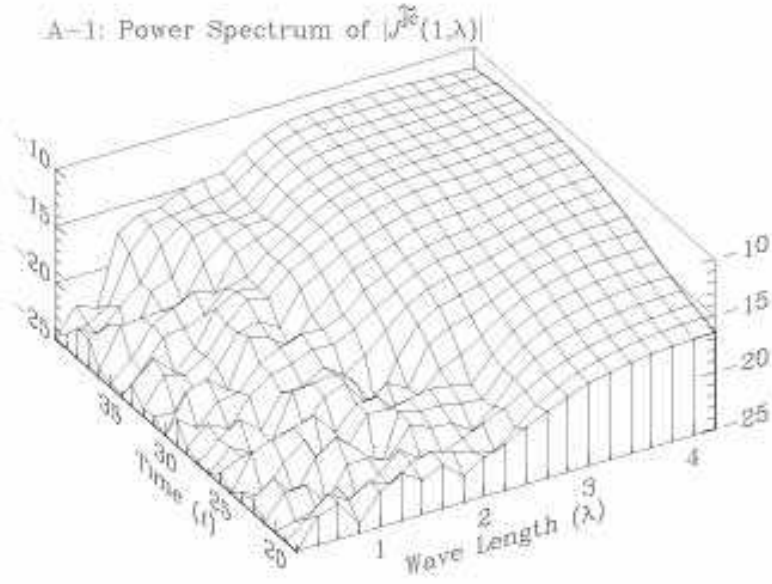
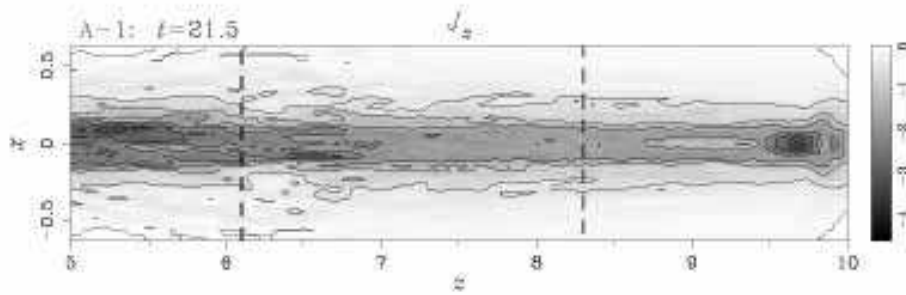


Fig. 17.— Analysis of the K–S criterion for Model A – 2 in the intermediate stage. (1) Space-time  $(\lambda, t)$  diagram of the Growing CD kink ( $m = 1$ ) mode showing the variation in growth with axial mode number ( $k = \lambda/2\pi$ ). (2) Enlarged snapshot of  $J_z$  ( $|x| \leq 0.635$ ,  $5.0 \leq z \leq 10.0$ ), similar to Figs. 10 and 12. The vertical arrows indicate the direction of transverse motion currently underway. (3) Transverse profiles (parallel to the  $x$ -axis) of the magnetic twist  $\Phi(r) \equiv \lambda|B_\phi|/rB_z$  (Left) and the toroidal Alfvén Mach number  $M_{A\phi}$  (Right) at the axial positions  $z = 6.1$  and  $8.3$ , indicated with the vertical dashed lines in panel (2). The horizontal lines in panel (3) indicate  $\Phi(r) = \Phi_{\text{crit}} = 2\pi$  (Left) and  $M_{A\phi} = 1$  (Right).

(1)



(2)



(3)

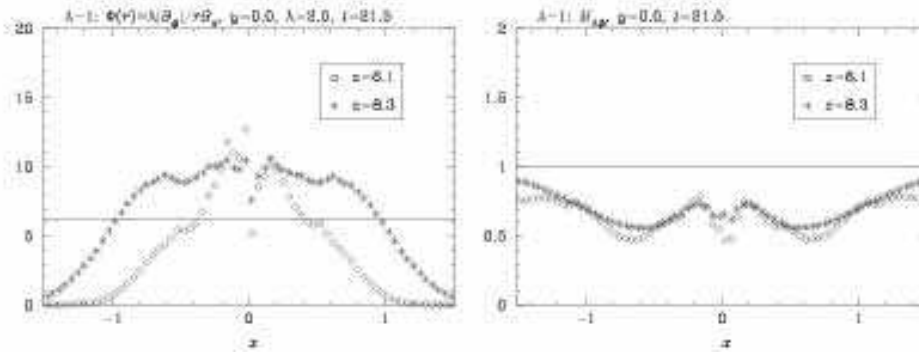


Fig. 18.— Similar to Fig. 17, but for Model A - 1.

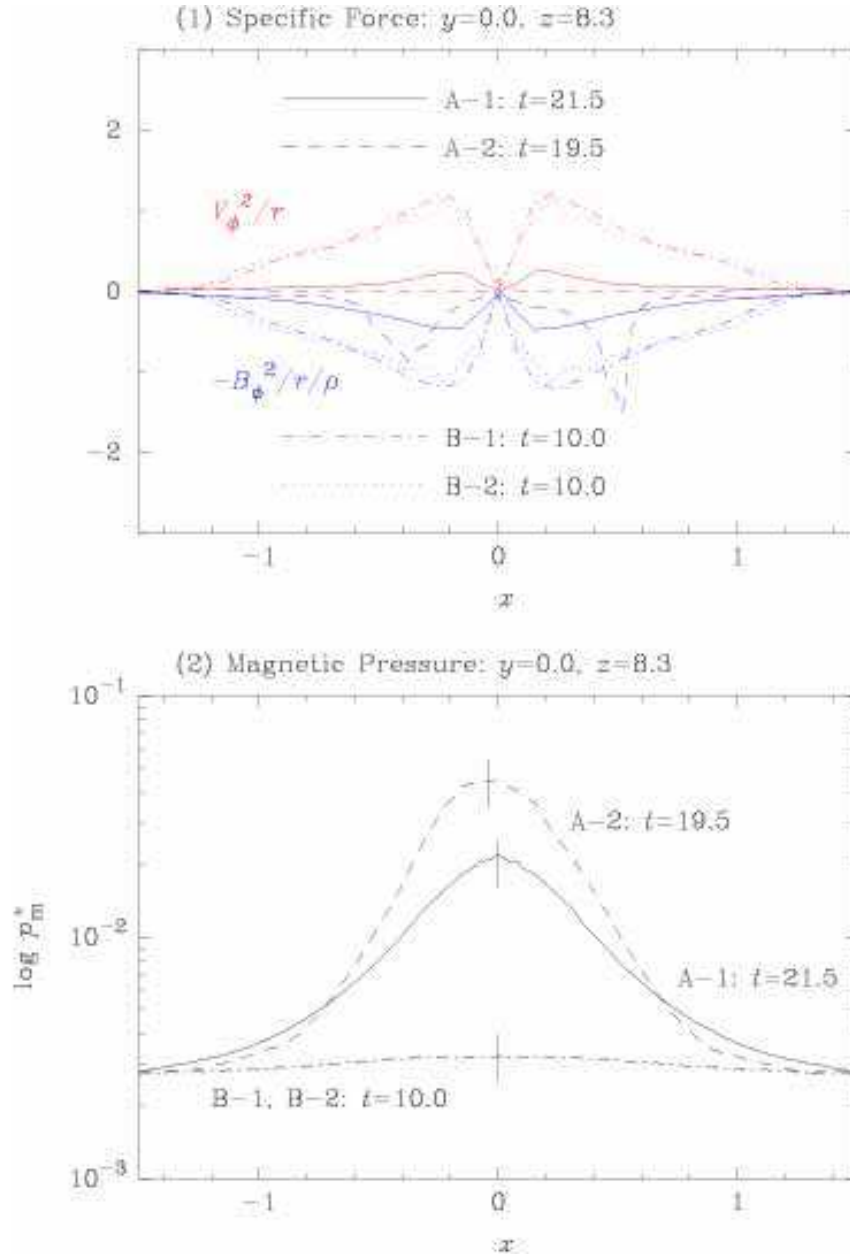


Fig. 19.— Transverse profiles (parallel to the  $x$ -axis) in the intermediate stage at axial position  $z = 8.3$ . (1) Profiles of the specific centrifugal force  $V_\phi^2/r$  (Red) and the specific hoop-stress  $-B_\phi^2/r/\rho$  (Blue). (2) Profiles of the magnetic pressure  $p_m^* = (B_\phi^2 + B_z^2)/2$  (logarithmic scale) for each of the models. (Note that the curves for models B – 1 and B – 2 coincide in the *dotted / dot-dashed* line in panel(2).) The short vertical solid lines in the *Lower* panel indicate the position of the peak of each transverse magnetic pressure profile.

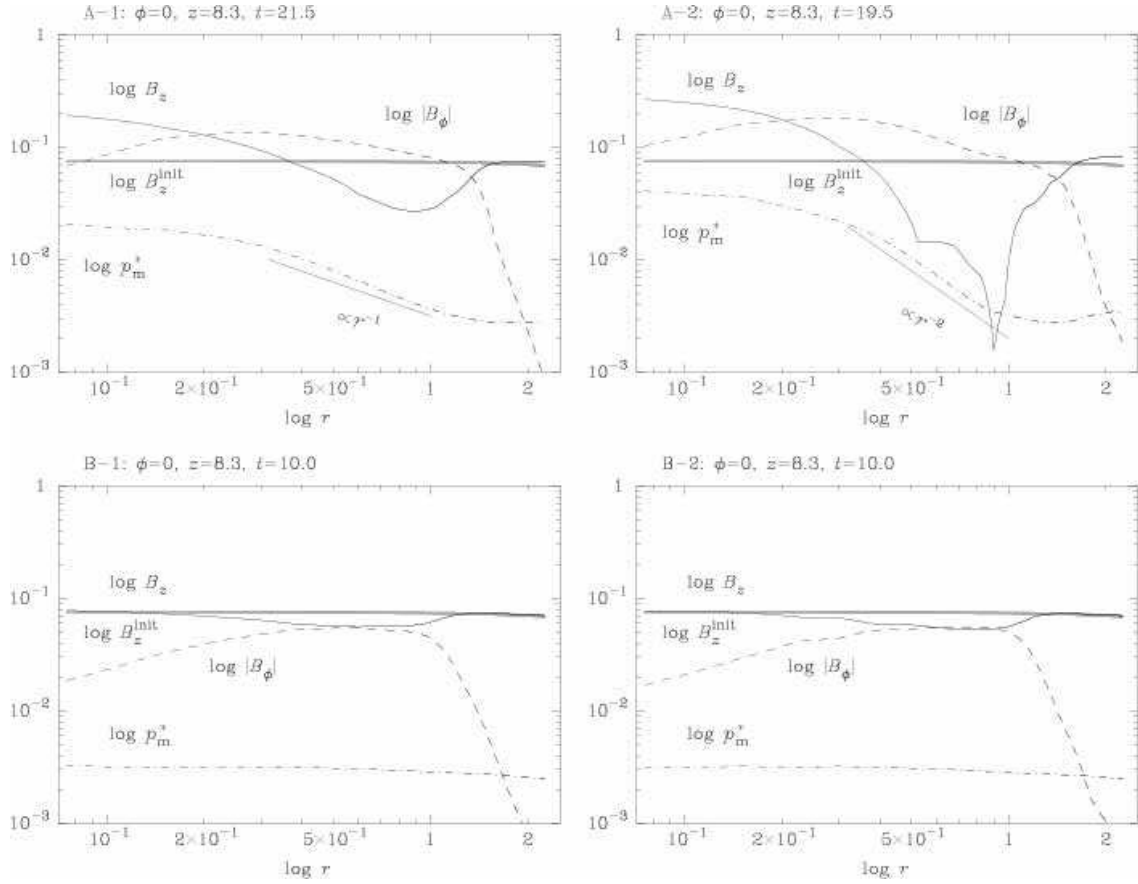


Fig. 20.— Radial profiles (parallel to the “ $r$ ”-axis along  $\phi = 0$ ) of the absolute value of magnetic field components  $B_z$ ,  $|B_\phi|$ , and the magnetic pressure  $p_m^*$  (logarithmic scale) in the intermediate stage at axial position  $z = 8.3$ .  $B_z^{\text{init}}$  (Light gray thick solid line) represents the initial ( $t = 0.0$ ) distribution of the axial field.

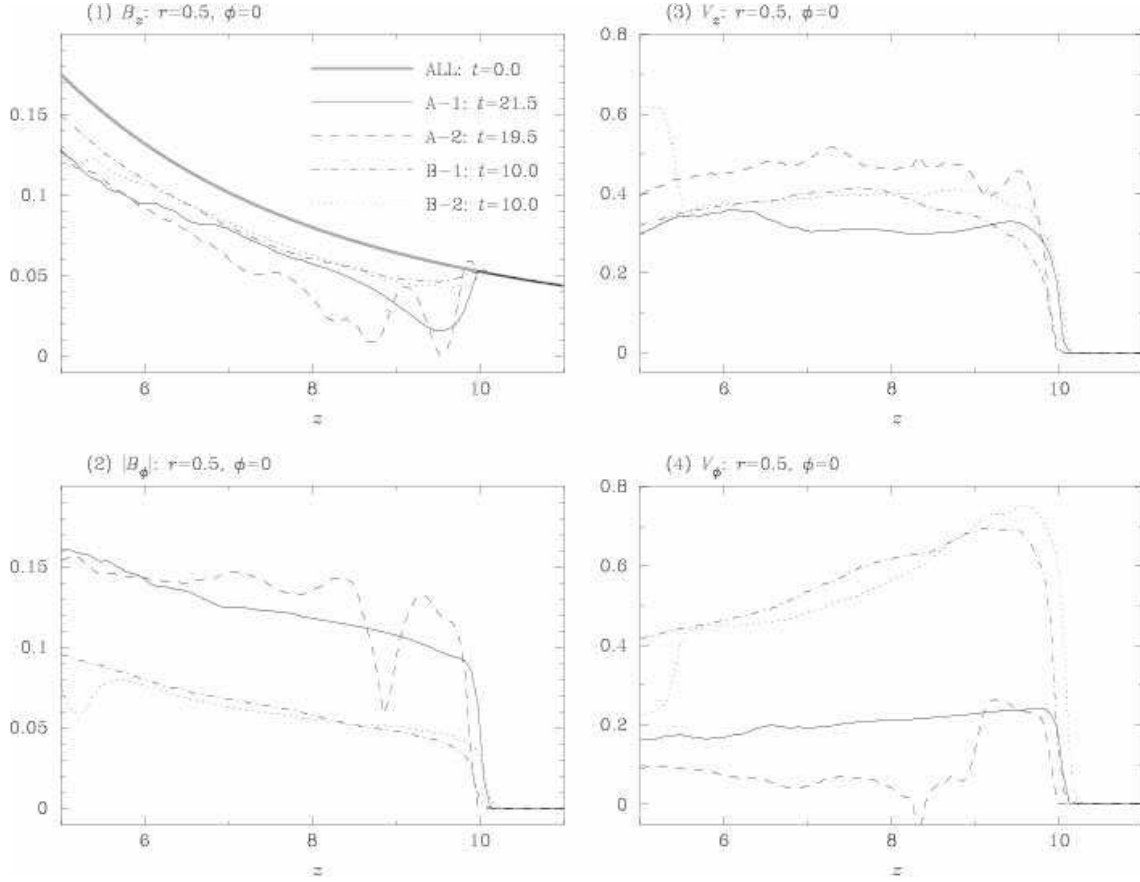


Fig. 21.— Offset axial profiles, parallel to the  $z$ -axis, at  $(r, \phi) = (0.5, 0)$  in the intermediate stage for each of the models. (1) Axial magnetic field component  $B_z$  (the initial distribution is also plotted by *light gray thick solid line*). (2) Absolute value of azimuthal magnetic field component  $|B_\phi|$ . (3) Axial velocity  $V_z$ . (4) Azimuthal velocity  $V_\phi$ .

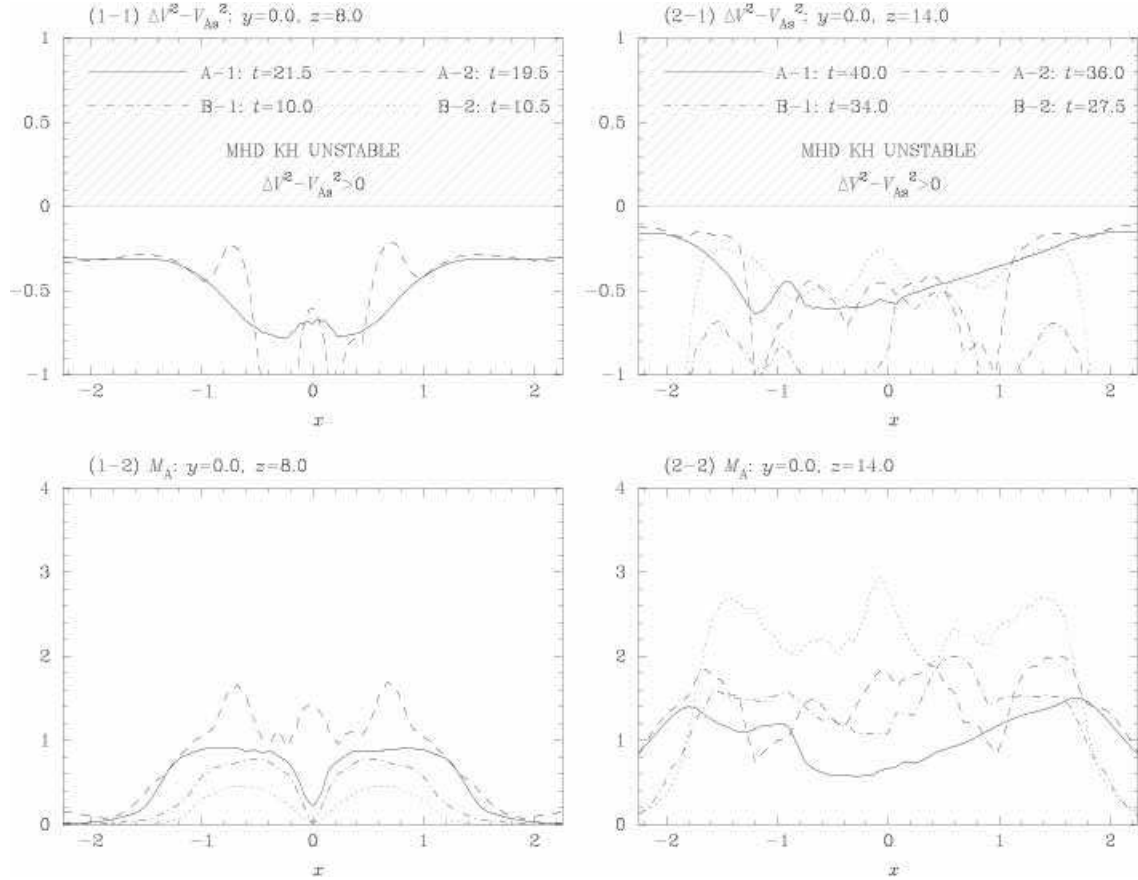


Fig. 22.— Transverse profiles in the  $x$  direction of velocity shear and Alfvén Mach number in the intermediate stage (*Left* panels at axial position  $z = 8.0$ ) and final stage (*Right* panels at  $z = 14.0$ ) of evolution. *Upper* panels: the difference between the square of the velocity shear  $\Delta V^2$  and the square of the surface Alfvén velocity  $V_{As}^2$ . *Lower* panels: the total Alfvén Mach number  $M_A$ . The shaded area in the *Upper* figures shows the MHD KH unstable region ( $\Delta V^2 \geq V_{As}^2$ ). In the first panel, models B – 1 and B – 2 do not appear, because their velocity difference lies below  $-1$ .

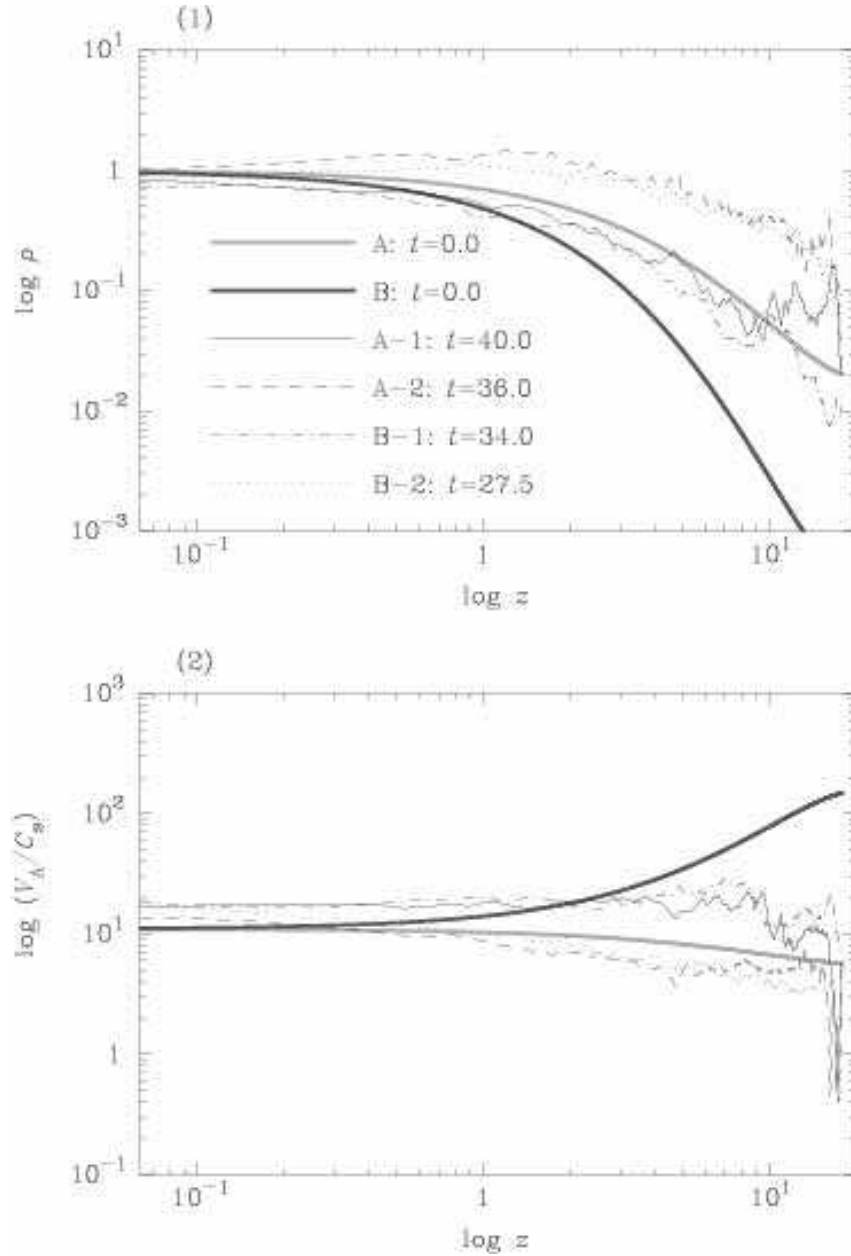


Fig. 23.— Axial profiles of (1) the density  $\rho$  (*Upper*) and (2) the ratio of Alfvén velocity to sound speed  $V_A/C_s$  (*Lower*) in the final stage of evolution. Each thick solid line represents the initial ( $t = 0.0$ ) distribution for Model A (*light gray*) and Model B (*dark gray*).

Table 1. Units of Physical Quantities for Normalization.

Physical Quantity	Description	Normalization Unit
$t$ .....	Time	$\tau_{A0} (\equiv L_0/V_{A0})$
$L (\equiv \sqrt{x^2 + y^2 + z^2})$	Length	$L_0$
$\rho$ .....	Density	$\rho_0$
$p$ .....	Pressure	$\rho_0 V_{A0}^2$
$\mathbf{V}$ .....	Velocity	$V_{A0}$
$\mathbf{B}$ .....	Magnetic field	$\sqrt{4\pi\rho_0 V_{A0}^2}$
$\mathbf{J}$ .....	Current Density	$\sqrt{4\pi\rho_0 V_{A0}^2}/L_0$

Note. — The initial value of the density  $\rho_0$  and Alfvén velocity  $V_{A0}$  at the origin  $(x, y, z) = (0, 0, 0)$  are chosen to be the typical density and velocity in the system. That is, the initial dimensionless density  $\rho'$  and Alfvén velocity  $V'_A$  at the origin are set to unity. The unit length scale  $L_0$  is approximately the same as the initial jet diameter at  $z = 0$ . So, we can define a characteristic time scale, the initial Alfvén crossing time  $\tau_{A0}$  at the origin, which is associated with  $L_0$  and  $V_{A0}$ . The time is normalized with  $\tau_{A0}$ , so the dimensionless Alfvén crossing time also is set to unity:  $\tau'_A = 1$ .

Table 2. Model Parameters and Flow Properties.

Model	$\alpha^a$	$\Gamma^b$	$\nabla C_s^b$	$\nabla V_A^d$	$\nabla \beta^e$	$F_{E \times B}/F_{\text{tot}}^f$
A-1 ..	1.0	5/3	$\searrow$	$\searrow$	$\nearrow$	$\sim 0.6$
A-2 ..	1.0	5/3	$\searrow$	$\searrow$	$\nearrow$	$\sim 0.9$
B-1 ...	2.0	5/3	$\searrow$	$\rightarrow$	$\searrow$	$\sim 0.6$
B-2 ...	2.0	5/3	$\searrow$	$\rightarrow$	$\searrow$	$\sim 0.9$

<sup>a</sup>Power index of  $\rho \propto |\mathbf{B}|^\alpha$ .

<sup>b</sup>Polytropic index of  $p \propto \rho^\Gamma$ .

<sup>c</sup>Gradient of the sound velocity along the  $z$ -axis.

<sup>d</sup>Gradient of the Alfvén velocity along the  $z$ -axis.

<sup>e</sup>Gradient of the plasma- $\beta$  along the  $z$ -axis.

<sup>f</sup>Time averaged Poynting flux  $F_{E \times B}$  injected into the system through the  $z = 0$  plane, normalized by the total energy flux  $F_{\text{tot}}$ .

Note. — Models A represent slowly decreasing atmospheres with decreasing  $V_A$ . Models B represent steeply decreasing atmospheres with constant  $V_A$ . The signs “ $\searrow$ ”, “ $\nearrow$ ”, and “ $\rightarrow$ ” indicate negative, positive, and no gradients along the  $z$ -axis, respectively.

Table 3. Comparison of Growth Rates for All Models.

Model	$\text{Im}(\omega)$	Growing azimuthal modes ( $m$ )	Saturation
A-1 ..	0.31	1, 2	No
A-2 ..	0.54	1	Yes
B-1 ...	0.51	1	No
B-2 ...	0.42	1	Yes